Published in final edited form as:

Nature. 2017 May 25; 545(7655): 452–456. doi:10.1038/nature22367.

Chromatin states define tumor-specific T cell dysfunction and reprogramming

Mary Philip[1], **Lauren Fairchild**[2,3], **Liping Sun**[4], **Ellen L. Horste**[1], **Steven Camara**[1], **Mojdeh Shakiba**[1,5], **Andrew C. Scott**[1,5], **Agnes Viale**[4], **Peter Lauer**[6], **Taha Merghoub**[5,7], **Matthew D. Hellmann**[5,8], **Jedd D. Wolchok**[5,7,9], **Christina S. Leslie**[2], and **Andrea Schietinger**[1,5]

[1]Immunology Program, Memorial Sloan Kettering Cancer Center, New York, NY 10065, USA

[2]Computational Biology Program, Memorial Sloan Kettering Cancer Center, New York, NY 10065, USA

[3]Tri-Institutional Training Program in Computational Biology and Medicine, Weill Cornell Medical College, New York, NY 10065, USA

[4]Integrated Genomics Operation, Center for Molecular Oncology, Memorial Sloan Kettering Cancer Center, New York, NY 10065, USA

[5]Weill Cornell Medical College, Cornell University, New York, NY 10065, USA

[6]Aduro Biotech, Inc., Berkeley, California 94720, USA

[7]Melanoma and Immunotherapeutics Service, Memorial Sloan Kettering Cancer Center, New York, NY 10065, USA

[8]Thoracic Oncology Service, Memorial Sloan Kettering Cancer Center, New York, NY 10065, USA

[9]Ludwig Center for Cancer Immunotherapy, Memorial Sloan Kettering Cancer Center, New York, NY 10065, USA

Abstract

Tumour-specific CD8 T cells in solid tumours are dysfunctional, allowing tumours to progress. The epigenetic regulation of T cell dysfunction and therapeutic reprogrammability (for example, to immune checkpoint blockade) is not well understood. Here we show that T cells in mouse tumours differentiate through two discrete chromatin states: a plastic dysfunctional state from which T cells can be rescued, and a fixed dysfunctional state in which the cells are resistant to reprogramming. We identified surface markers associated with each chromatin state that distinguished reprogrammable from non-reprogrammable PD1^{hi} dysfunctional T cells within

Supplementary Information is available in the online version of the paper.

Author Contributions: M.P. and A.S. conceived and designed the study, carried out experiments, analyzed, and interpreted data. L.F. designed and performed all high-throughput computational analyses; C.S.L. designed and supervised computational analyses; E.H., S.C., M.S., and A.C.S. assisted with experiments; L.S. and A.V. performed ATAC-Seq; P.L. generated *Listeria* strains, T.M., M.H. and J.D.W. provided human samples. M.P. and A.S. wrote the manuscript, with all authors contributing to writing and providing feedback.

Author Information: The authors declare no competing financial interest.

heterogeneous T cell populations from tumours in mice; these surface markers were also expressed on human PD1^{hi} tumour-infiltrating CD8 T cells. Our study has important implications for cancer immunotherapy as we define key transcription factors and epigenetic programs underlying T cell dysfunction and surface markers that predict therapeutic reprogrammability.

Introduction

Tumor-specific CD8 T cells (TST) are often found within solid tumors, but tumors progress despite their presence, suggesting that these TST are dysfunctional[1]. The clinical success of immune checkpoint blockade (e.g. PD1/PDL1, CTLA4 blocking antibodies) and adoptive T cell therapy in a subset of cancer patients demonstrates the great potential of TST[2]; however, important questions remain, including how to predict which patients will respond to therapy and precisely which TST mediate clinical responses[3–5]. Moreover, an unmet need is the development of interventions for tumors refractory to checkpoint blockade despite having ample TST infiltration.

We previously demonstrated that early during tumorigenesis, TST become non-responsive, exhibiting the phenotypic, functional, and transcriptional features of tumor-reactive tumor-infiltrating lymphocytes (TIL) from late-stage human solid tumors[6]. TST dysfunction is initially reversible but ultimately becomes irreversible, even after removal of dysfunctional T cells from the tumor microenvironment and multiple rounds of cell division[6]. We hypothesized that this heritable, signal-independent dysfunctional state is epigenetically imprinted. The epigenetic programs that regulate normal differentiation of innate and adaptive lymphocytes have been described[7–10]. However, the epigenetic programs regulating T cell differentiation and dysfunction in tumors are not known. In this study, we used the "Assay for Transposase Accessible Chromatin using Sequencing" (ATAC-Seq)[11] to assess genome-wide chromatin accessibility changes during T cell differentiation in tumors compared to acute infection.

CD8 T cell chromatin changes during infection

We transferred congenically-marked naïve (N; CD44^{lo} CD62L^{hi}) TCR_{TAG} from TCR_{TAG} transgenic mice (specific for SV40 large T antigen epitope I (TAG))[12] into wild-type C57BL/6 mice, which were immunized one day later with recombinant *Listeria monocytogenes* strain expressing TAG (*Lm*TAG)[6,13]. TCR_{TAG} were re-isolated, phenotypically and functionally characterized, and subjected to ATAC-Seq and RNA-Seq at 5, 7 (effectors; E5, E7) and 60+ days (memory; M) after immunization (Fig. 1a). N, E5, E7 and M expressed characteristic activation, homing and cytokine receptors (CD44, CD62L, IL7R), transcription factors (TFs) (TBET), cytotoxic molecules (GZMB, CD107), and pro-inflammatory cytokines (IFN-γ and TNF-α) (Extended Data Fig. 1).

ATAC-Seq libraries generated from N, E5, E7, and M showed the expected distribution of fragment lengths (Extended Data Fig. 2). Using DESeq2[14] to assess differential chromatin accessibility, we found that dramatic chromatin remodeling occurred as N differentiated to the effector state (E5), with much less remodeling from E5 to E7 and E7 to M (Fig. 1b, c, and Extended Data Fig. 3a). In N, effector gene loci such as *Prf1* and *Tnf* shared highly

accessible chromatin and basal transcriptional activity with E5/E7 and M (Extended Data Fig. 3b), consistent with activating histone marks previously shown at these loci in naïve T cells[15,16].

We analyzed accessibility changes during the N to E5 transition in loci associated with early and late TCR-response genes as defined by the Immunological Genome Project[17]. Early-response genes showed much fewer changes compared to late-response genes (Extended Data Fig. 3c). For example, *Ldha*, (encoding LDHA, needed for the metabolic shift to aerobic glycolysis and IFNγ production[18]), and *Mki67* (encoding KI67, required for chromosome segregation during mitosis[19]), require no change in chromatin accessibility to be rapidly induced after TCR stimulation (Extended Data Fig. 3d).

Memory T cells exhibit more rapid and robust effector function upon antigen re-encounter compared to naïve T cells[20]. K-means clustering of RNA expression patterns (Fig. 1d, left) revealed two trends: transient gene activation or down-regulation in E5/E7 but not M (clusters 1, 2, 5, 6), and stable gene activation or down-regulation in E5, E7, and M (clusters 3 and 4). In contrast, chromatin accessibility for these loci was largely similar in E5/E7 and M (Fig. 1d, middle). Thus, the “effector-like” accessibility in M permits basal transcription of certain effector genes (cluster 3) such as *Ifng*, while other genes are transcriptionally silent but poised for rapid re-expression upon TCR activation (cluster 1, *Gzma*) (Fig. 1d, right).

Chromatin state dynamics of TST dysfunction

We next assessed chromatin state dynamics in TST over the course of tumorigenesis using the previously described tamoxifen (Tam)-inducible, autochthonous liver cancer model (ASTxCre-ER^{T2}; Cre-ER^{T2} = Tam-dependent Cre-recombinase) in which TAG is a tumor-specific antigen[6]. ASTxCre-ER^{T2} mice initially develop pre-malignant lesions which eventually progress into hepatocellular carcinoma (HCC; by day 60–90)[6]. We transferred congenically-marked naïve TCR$_{TAG}$ (N, identical to N in Fig. 1a) into ASTxCre-ER^{T2} mice 1 day prior to Tam and then analyzed TCR$_{TAG}$ at different time points (Fig. 2a). Liver-infiltrating TCR$_{TAG}$ downregulated CD62L, uniformly expressed activation markers CD44 and inhibitory receptors PD1 and LAG3, and failed to produce IFNγ or TNFα (Fig. 2b). Massive chromatin remodeling occurred by day 5, followed by a second wave of remodeling between days 7 and 14 (Fig. 2c, d and Extended Data Fig. 4a). Strikingly, after the second wave, few accessibility changes occurred, even after progression to established tumors at day 60+ (Fig. 2c, d, e). Thus, TST differentiated through two discrete chromatin states: an initial dysfunctional state 1 (L5, L7), and later dysfunctional state 2, established by day 14 and persisting thereafter. Many of the ATAC-Seq peaks gained or lost were in intronic and intergenic regions (potential enhancer peaks), while peaks present in all CD8 T cells were in promoter regions (Extended Data Fig. 4b, bottom); this pattern was also seen in functional CD8 T cell differentiation (Extended Data Fig. 4b, top).

TCR$_{TAG}$ in malignant lesions followed a distinct epigenetic trajectory compared to TCR$_{TAG}$ in acute infection (L5 versus E5; Fig. 2d), and many peak changes were unique to either the early dysfunctional (L5) or functional (E5) state (Extended Data Fig. 4c) and included TCR

signaling and cytokine production pathway genes (Extended Data Fig. 4d). Enhancer peaks in the *Ifng* locus that opened during normal effector differentiation were inaccessible in dysfunctional TCR_{TAG} (Fig. 2f, right). An intergenic peak near (−23.8 kb) the *Pdcd1* (PD1-encoding) locus was uniquely accessible in L5 to L60+ but not in E5/E7 and M (Fig. 2f, left); a similar peak was described in exhausted T cells in chronic viral infection[21–23]. We tested whether accessibility of potential TF targets changed preferentially during differentiation from N to L5 as compared to N to E5 (Extended Data Fig. 5a). Predicted NFATC1 binding sites, including those in genes encoding inhibitory receptors and negative regulators such as *Ctla4, Pdcd1*, *Tigit, Socs1*, and *Cblb* and TF *Egr1* and *Egr2*, had increased peak accessibility in dysfunctional L5 (Extended Data Fig. 5a, b). NFAT TF family members, particularly NFATC1 and NFATC2, are important regulators of T cell development and function (reviewed in[24]), as well as exhaustion in chronic viral infections[25]. While some genes with increased NFATC1 peak accessibility in L5 showed immediate transient transcriptional activation, others were activated later (Extended Data Fig. 5c). TF footprints could be identified for NFATC1 as well as other TFs (Extended Data Fig. 6a).

Chromatin states are associated with reprogrammability

Intriguingly, the discrete chromatin states in dysfunctional TCR_{TAG} correlated temporally with our previous observation that L8 but not L35 were capable of regaining effector function[6]. Indeed, when we re-isolated TCR_{TAG} from liver lesions and cultured them *in vitro* with IL15 (Fig. 3a), previously shown to induce proliferation and restore effector function in tumor-reactive CD8 T cells[26,27], L5 and L7 regained the ability to produce IFNγ and TNFα, but TCR_{TAG} isolated at day 12 and after did not (Fig. 3a). Thus state 1 dysfunction is plastic, but with further chromatin remodeling between days 7 and 14, becomes fixed (state 2).

Chromatin peaks with TCF family motifs closed during the state 1 (L7) to state 2 (L14) transition, while E2F, ETS, and KLF family TF motif-containing peaks opened (Fig. 3b). Indeed, TCF1 (encoded by *Tcf7*) protein levels decreased between L7 and L14 (Extended Data Fig. 6b), and analysis of closing peaks showed enrichment for WNT receptor signaling pathway genes, upstream of TCF family TFs, as well as cytokine response, TCR signaling, and T cell differentiation pathway genes (Extended Data Fig. 6c). Among the TCR signaling genes most up-regulated during the L7-L14 transition were negative regulators such as *Cish1* and *Socs2*, while co-stimulatory molecule genes such as *Icos* and *Cd28* were down-regulated together with closing of multiple peaks within their loci (Extended Data Fig. 6d).

We next used an *in vivo* pharmacologic strategy to test the role of NFAT and TCF in TST dysfunction. FK506 is an immunosuppressant that inhibits NFAT nuclear translocation and downstream gene activation[28,29], and we used 25% of the full immunosuppression dose to partially downregulate NFAT activity without completely blocking T cell activation/effector function. TWS119, a GSK3β inhibitor, enhances CD8 memory differentiation through WNT/TCF1 activation[30], so we treated TCR_{TAG}-adoptively transferred ASTxCre-ER^{T2} mice with FK506 alone or in combination with TWS119 (Extended Data Fig. 7a). Indeed, L10 TST from FK506 and FK506/TWS119-treated mice had decreased expression of NFATC1-targets PD1 and LAG3, increased levels of TCF1 and EOMES (Extended Data

Fig. 7b), and were more efficiently reprogrammable (Extended Data Fig. 7c) compared to controls or TWS119 alone (data not shown).

Surface proteins associated with chromatin states

We then looked for cell surface proteins whose expression correlated with chromatin states 1 or 2 and thus might predict reprogrammability of heterogeneous TIL. PD1 and LAG3 were similarly expressed by both plastic (L5, L7) and fixed (L14+) dysfunctional TST (Fig. 2b) and thus not informative in this regard. We identified membrane protein genes differentially expressed between early (L5, L7) and late (L14 to L60+) dysfunctional TCR_{TAG} (Fig. 3c) and found several markers not previously associated with tumor-induced T cell dysfunction. State 1 (L5, L7) TCR_{TAG} had low expression of CD38, CD101, and CD30L and high expression of CD5, while state 2 (L14, L28) TCR_{TAG} had the opposite pattern (Fig. 3d). Consistent with its expression, the *Cd38* locus contained intergenic and intronic peaks uniquely accessible in state 2 TST (Extended Data Fig. 8a). TCF1 downregulation coincided with CD38 upregulation (Extended Data Fig. 8b), and other key regulators of CD8 T cell differentiation such as IRF4 and BCL2 showed a similar binary expression in early and late TST (Extended Data Fig. 8c). Moreover, TCR_{TAG} from FK506 and FK506/TWS119-treated mice expressed low CD38 and CD101 compared to controls, correlating with their improved reprogrammability (Extended Data Fig. 7d). To test whether these markers could identify reprogrammable T cells within a heterogeneous TST population, we sorted $CD38^{lo}/CD101^{lo}$ and $CD38^{hi}/CD101^{hi}$ TST in L14 populations and assessed reprogrammability (3 days *in vitro* IL-15). While $CD38^{lo}/CD101^{lo}$- L14 regained the ability to produce IFNγ and TNFα, $CD38^{hi}/CD101^{hi}$- L14 did not (Fig. 3e).

We asked whether these findings could be applied to other tumor histologies and/or T cell specificities by utilizing murine B16F10 (B16) melanoma expressing ovalbumin (B16-OVA), a model antigen recognized by OVA-specific OT1 CD8 T cells (TCR_{OT1}). Naïve congenically-marked TCR_{OT1} were adoptively transferred into B16-OVA tumor-bearing B6 mice. Tumor-infiltrating TCR_{OT1} upregulated CD44, PD1, and LAG3, downregulated CD62L, and lost the ability to produce IFNγ or TNFα (Extended Data Fig. 8d). Later dysfunctional TCR_{OT1} expressed high levels of CD38, CD101 and downregulated CD5 compared to early dysfunctional D5-TCR_{OT1} (Extended Data Fig. 8e). Moreover, late dysfunctional D21-TCR_{OT1} could not regain the ability to produce IFNγ or TNFα, in contrast to early dysfunctional D5-TCR_{OT1} (Extended Data Fig. 8f).

Memory T cells enter state 2 dysfunction in tumors

We next tested if the “functionally-poised” chromatin state present in memory T cells (M; Fig. 1) could prevent them from becoming dysfunctional in tumors. M (TCR_{TAG}) were transferred into ASTxAlb:Cre mice[6] bearing established HCC and one day later immunized with *Lm*TAG (Fig. 4a). By day 7, tumor-infiltrating M (ML7) rapidly upregulated PD1 and LAG3 and progressively lost effector function (Fig. 4b and Extended Data Fig. 9a). ATAC-Seq revealed that M followed a similar epigenetic trajectory as N in early malignant lesions (Fig. 4c and Extended Data Fig. 9b-d), and remarkably, by day 35, the chromatin state of transferred M was nearly identical to that of N at day 35 in early malignant lesions (ML35

and L35; Fig. 4d). Dysfunctional M displayed the same gain and loss of ATAC-Seq peaks in critical gene loci including *Pdcd1*, *Ctla4*, *Cd38*, *Tcf7*, and *Ifng* (Extended Data Fig. 9e). Changes in surface protein expression (CD38, CD101, CD30L, and CD5) between ML7 and ML14 were like those seen with N (L7 and L14, respectively) (Extended Data Fig. 9f). We obtained similar results when *Lm*TAG immunization after adoptive transfer was omitted (Extended Data Fig. 9b–d).

Chromatin accessibility in human TIL

Finally, we examined chromatin states of human CD8 tumor-infiltrating lymphocytes (TIL) and peripheral blood lymphocytes (PBL) from healthy donors. We carried out ATAC-Seq on naïve (N; CD45RA+ CD45RO-), effector memory (EM; CD45RA- CD45RO+ $CD62L^{lo}$) and central memory (CM; CD45RA- CD45RO+ $CD62L^{hi}$) CD8 PBL from healthy donors and $PD1^{hi}$ CD8 TIL isolated from human melanoma and non-small cell lung tumors (NSCLC) (Extended Data Fig. 10a). Human N had a distinct chromatin state as compared to EM and CM, which were similar (Fig. 5a and Extended Data Fig. 10b) though distinct accessibility patterns in genes such as *SELL* (encoding CD62L) distinguished all three states (Extended Data Fig. 10c). $PD1^{hi}$ TIL uniquely gained and lost multiple peaks, for example in *IFNG*, *EGR2, CD5*, and *CTLA4* (Extended Data Fig. 10d). We compared the non-promoter peak changes that occurred during functional and dysfunctional mouse CD8 T cell differentiation with those observed in human PBL and $PD1^{hi}$ TIL and found that human $PD1^{hi}$ TIL had the greatest overlap in peak accessibility changes with fixed dysfunctional (state 2) murine TST (Fig. 5b). For example, the *TCF7*/*Tcf7* locus showed similar intergenic and intronic peak accessibility changes in human $PD1^{hi}$ TIL and murine state 2 TCR_{TAG} (Fig. 5c). A subset of $PD1^{hi}$ TIL expressed higher levels of CD38 /CD101 and lower levels of CD5 (Fig. 5d), suggesting that these markers could potentially be used to identify T cells amenable to therapeutic reprogramming in human tumors.

Discussion

In this study, we define for the first time the chromatin state dynamics underlying tumor-specific T cell dysfunction over the course of tumorigenesis. Naïve TST encountering tumor antigen in pre-malignant lesions differentiated to an initially plastic, therapeutically reprogrammable chromatin state, then transitioned to a fixed dysfunctional chromatin state that did not undergo further remodeling, even with progression to large established tumors (Extended Data Fig. 10e). The rapid induction of dysfunction early during tumorigenesis without progression through an effector state resembles peripheral tolerance induction[31,32]. We identified core elements shared between murine fixed dysfunctional TST and human $PD1^{hi}$ TIL. Surprisingly, memory TST differentiated to the same fixed dysfunctional chromatin state in tumors, suggesting that antigen exposure in tumors can overwrite pre-existing epigenetic programs regardless of the initial differentiation state.

We identified surface markers, including CD101 and CD38, which were associated with discrete dysfunctional chromatin states and demarcated reprogrammable from non-reprogrammable $PD1^{hi}$ T cells within heterogeneous TIL populations, a finding of important potential clinical relevance, and human $PD1^{hi}$ TIL showed heterogeneous expression of

these markers. In patients who do not respond to immune checkpoint blockade (non-responders), PD1^{hi} TIL may be in a fixed dysfunctional state, in contrast to responders whose PD1^{hi} TIL are in a plastic state, amenable to reprogramming. Our studies on the epigenetic and transcriptional programs underlying TST dysfunctional states and therapeutic reprogrammability point to new targets and strategies to transform TST into potent anti-tumor agents.

METHODS

Mice

TCR_{TAG} transgenic mice (B6.Cg-Tg(TcraY1,TcrbY1)416Tev/J)[12], Cre-ER^{T2} (B6.129-Gt(ROSA)26Sor$^{tm1(cre/ERT2)Tyj}$/J), Alb:Cre (B6.Cg-Tg(Alb-cre)21Mgn/J), TCR-OT1 (C57BL/6-Tg(TcraTcrb)1100Mjb/J), Ly5.1 (B6.SJL-Ptprc^{a} Pepc^{b}/BoyJ), and C57BL/6J Thy1.1 mice were purchased from The Jackson Laboratory. TCR_{TAG} mice were crossed to Thy.1.1 mice to generate TCR_{TAG} Thy.1.1 mice. TCR-OT1 were crossed to Ly5.1 mice to generate TCR-OT1 Ly5.1 mice. AST [Albumin-floxStop-SV40 large T antigen (TAG)][33] were crossed to Cre-ER^{T2} or Alb:Cre mice to obtain ASTxCre-ER^{T2} and ASTxAlb:Cre mice respectively[6]. Both female and male mice were used for studies. Mice were age- and sex-matched and between 1.5 - 3 months old when used for experiments. Animals were assigned randomly to experimental groups. All mice were bred and maintained in the animal facility at Memorial Sloan Kettering Cancer Center (MSKCC). Experiments were performed in compliance with the MSKCC Institutional Animal Care and Use Committee (IACUC) regulations.

Antibodies and reagents

Fluorochrome-conjugated antibodies were purchased from BD Biosciences, eBioscience, Biolegend, and Cell Signaling Technology. Tamoxifen (Sigma) stock solution was prepared by warming tamoxifen in 1ml sterile corn oil at 50°C for 15 minutes, then further diluted in corn oil to obtain the stock concentration (5mg/ml in corn oil). A single dose of tamoxifen (1 mg) was administered intraperitoneally (i.p.) into ASTxCre-ER^{T2} mice.

Intracellular cytokine staining

Intracellular cytokine staining was performed using the Cytofix/Cytoperm Plus kit (BD Biosciences) per the manufacturer's instructions. Briefly, T cells were mixed with 2×10^{6} congenically-marked splenocytes and incubated with Tag-I peptide (0.5 μg/ml) or OVA peptide (0.1 μg/ml) for 4–5 hours at 37°C in the presence of GolgiPlug (brefeldin A). After staining for cell-surface molecules, the cells were fixed, permeabilized, and stained with antibodies to IFN-γ (XMG1.2) and TNF-α (MP6-XT22).

Flow cytometric analysis

Flow cytometric analysis was performed using Fortessa and LSR FACS analyzers (BD Biosciences, San Jose, CA); cells were sorted using BD FACS Aria (BD Biosciences, San Jose, CA) at the MSKCC Flow Core Facility. Flow data were analyzed with FlowJo v. 10 software (Tree Star Inc, Ashland, OR).

Listeria infection

The *Listeria monocytogenes* (*Lm*) Δ*actA* Δ*inlB* strain[13] expressing the Tag-I epitope (SAINNYAQKL, SV40 large T antigen$_{206\text{-}215}$) was generated by Aduro Biotech as previously described[34]. Experimental vaccination stocks were prepared by growing bacteria to early stationary phase, washing in phosphate buffered saline, formulated at approximately 1×10^{10} colony forming units (cfu)/ml, and stored at −80°C. Mice were infected i.p. with 5×10^{6} cfu of *Lm*TAG.

Adoptive T cell transfer

For the generation of effector and memory TCR_{TAG} $CD8^+$ T cells, 10^5 $CD8^+$ splenocytes from TCR_{TAG} Thy1.1 transgenic mice were adoptively transferred into B6 (Thy1.2) mice; one day later, mice were infected with 5×10^{6} cfu *Lm*TAG. Effector TCR_{TAG} $CD8^+$ T cells were isolated from the spleens of B6 host mice and analyzed 5 or 7 days post *Lm*TAG immunization; memory TCR_{TAG} $CD8^+$ T cells were isolated from spleens of B6 host mice and analyzed at least 2–3 months post *Lm*TAG immunization. For the transfer of naïve TCR_{TAG} T cells into ASTxCre-ER^{T2} mice, 1×10^{5} – 2.5×10^{6} $CD8^+$ splenocytes from TCR_{TAG} Thy1.1 transgenic mice were adoptively transferred into ASTxCre-ER^{T2} mice; 1 day later, mice were treated with 1mg tamoxifen and donor T cells isolated for subsequent analyses. For memory TCR_{TAG} transfer experiments $3\text{–}4\times10^{4}$ TCR_{TAG} $Thy1.1^+$ $CD44^{hi}$, $CD62L^{hi}$ sorted central memory CD8 T cells were adoptively transferred into ASTxAlb:Cre mice; one day later, mice were infected with 5×10^{6} cfu *Lm*TAG (10^5 central memory T cells were sorted and transferred for experiments without subsequent listeria immunization).

B16-OVA tumor model

5×10^{5} – 1×10^{6} B16 tumor cells expressing OVA (full-length or cytosolic as previously described[35]) were injected into C57BL/6J wild-type mice. Once tumors were established (1–2 weeks later) naïve Ly5.1 congenically-marked TCR_{OT1} CD8 T cells were adoptively transferred and isolated from tumors at indicated time points. Tumor volumes did not exceed the permitted volumes specified by the MSKCC IACUC protocol. The B16 cell line was obtained from ATCC. It was tested negative for all rodent pathogens including Mycoplasma pulmonis.

Cell isolation for subsequent analyses

Spleens were mechanically disrupted with the back of a 3-ml syringe, filtered through a 70-μm strainer, and red blood cells (RBC) were lysed with ammonium chloride potassium buffer. Cells were washed twice with cold RPMI 1640 media supplemented with 2μM glutamine, 100U/ml penicillin/streptomycin, and 5–10% FCS (cRPMI). Liver tissue was mechanically disrupted to a single cell suspension using a 150 μ metal mesh and glass pestle in ice-cold 3% FCS/HBSS and passed through a 70 μm strainer. The liver homogenate was spun down at 400 g × 5 minutes at 4°C, and the pellet was resuspended in 30ml 3% FCS/HBSS, 500ul (500U) heparin, and 17ml Percoll (GE), mixed by inversion, and spun at 500 g × 10 min at 4°C. Pellet was lysed with ammonium chloride potassium buffer and cells were further processed for downstream applications.

IL15 *in vitro* culture

TCR_{TAG} or TCR_{OTI} were isolated from tumors at various time points post transfer and cultured *in vitro* in the presence of IL15 (100ng/ml) in cRPMI for 3–4 days.

Pharmacologic rescue studies

Naïve TCR_{TAG} ($Thy1.1^+$) were transferred into ASTxCre-ER^{T2} ($Thy1.2^+$) mice which were treated with tamoxifen one day later. On days 2–9 mice were treated with the calcineurin inhibitor FK506 (Prograf, 5 mg/ml) (2.5mg/kg/mouse i.p. once daily) alone, or in combination with the GSK3β inhibitor TWS119 (Sigma; 0.75mg/mouse i.p. once daily; days 5–8). Control mice were treated with PBS and/or DMSO.

Human samples

Human tumor samples and healthy donor peripheral blood lymphocytes were obtained as per protocols approved by the MSKCC Institutional Review Board (IRB), and all patient and healthy donors provided informed consent. Peripheral blood lymphocytes were flow-sorted for naïve, effector memory-like and central memory-like phenotypes as described in Extended Data Fig. 10a. Human melanoma and lung tumors were mechanically disrupted as described for solid murine tumors, and CD45RO+ PD^{hi} CD8+ T cells were flow-sorted for subsequent ATAC-Seq analysis.

Statistical analyses

Statistical analyses on flow cytometric data were performed using unpaired two-tailed Student's *t* tests (Prism 6.0, GraphPad Software). A *P* value of <0.05 was considered statistically significant.

Sample preparation for ATAC-Seq and RNA-Seq

Mouse samples—Replicate samples were isolated from spleens or livers and sorted as follows:

- **i.** Naïve TCR_{TAG} $Thy1.1^+$ T cells were sorted by flow cytometry ($CD8^+/CD44^{lo}$) from spleens of TCR_{TAG}Thy1.1 transgenic mice.
- **ii.** D5 and D7 effector, and memory TCR_{TAG} $Thy1.1^+$ T cells were sorted by flow cytometry ($CD8^+/Thy1.1^+$) from spleens of infected B6 (Thy1.2) host mice (see above) 5 and 7 days, or 2–3 months post listeria infection.
- **iii.** $TCR_{TAG}Thy1.1^+$ T cells from pre-/early malignant liver lesions: naïve TCR_{TAG} $Thy1.1^+$ T cells were adoptively transferred into ASTxCre-ER^{T2} mice. 1 day later, mice were given 1mg tamoxifen i.p. At given time points post tamoxifen treatment, T cells were isolated and sorted ($CD8^+/Thy1.1^+$) from livers as described above.
- **iv.** TCR_{TAG} $Thy1.1^+$ memory T cells from established hepatocellular carcinomas in ASTxAlb:Cre mice: TCR_{TAG} memory T cells were isolated from tumors and flow sorted ($CD8^+/Thy1.1^+$) as described above.

Human samples—Samples were flow-sorted as described in Extended Data Fig. 10a.

After flow-sorting, all samples for downstream ATAC-Seq analysis were frozen in 10% DMSO/FCS and stored at −80°C; samples for RNA-seq were directly sorted into Trizol and frozen and stored at −80°C.

Transcriptome Sequencing

RNA from sorted cells was extracted using RNeasy mini kit (Qiagen) per instructions provided by the manufacturer. After ribogreen quantification and quality control of Agilent BioAnalyzer, 6–15 ng of total RNA underwent amplification (12 cycles) using the SMART-seq V4 (Clontech) ultralow input RNA kit for sequencing. 10ng of amplified cDNA was used to prepare Illumina hiseq libraries with the Kapa DNA library preparation chemistry (Kapa Biosystems) using 8 cycles of PCR. Samples were barcoded and run on a Hiseq 2500 1T in a 50bp/50bp Paired end run, using the TruSeq SBS Kit v3 (Illumina). An average of 51 million paired reads were generated per sample and the percent of mRNA bases was 62.5% on average.

ATAC Sequencing

Chromatin profiling was performed by ATAC-Seq as described previously[11]. Briefly, 12,000 to 50,000 cells were washed in cold PBS and lysed. Transposition was performed at 42°C for 45 min. After purification of the DNA with the MinElute PCR purification kit (Qiagen), material was amplified for 5 cycles. Additional PCR cycles were evaluated by real time PCR. Final product was cleaned by Ampure Beads at a 1.5× ratio. Libraries were sequenced on a Hiseq 2500 1T in a 50bp/50bp Paired end run, using the TruSeq SBS Kit v3 (Illumina). An average of 47×10^6 paired reads were generated per sample.

ATAC data and preprocessing

Raw ATAC-Seq reads were trimmed and filtered for quality using Trim Galore! v0.4.0 (http://www.bioinformatics.babraham.ac.uk/projects/trim_galore/), powered by CutAdapt v1.8.1 (http://dx.doi.org/10.14806/ej.17.1.200) and FastQC v0.11.3 (http://www.bioinformatics.babraham.ac.uk/projects/fastqc/). Paired-end reads were aligned using Bowtie2 v2.2.5[36] against either mm10 or hg38 and non-uniquely mapping reads were removed. To correct for the fact that the Tn5 transposase binds as a dimer and inserts two adapters in the Tn5 tagmentation step[37], all positive-strand reads were shifted 4bp downstream and all negative-strand reads were shifted 5bp upstream to center the reads on the transposon binding event[11]. We then pooled the shifted reads by sample type and identified peaks using MACS2[38] with a threshold of FDR-corrected $P < 1e\text{-}2$ using the Benjamini-Hochberg procedure for multiple hypothesis correction. As called peaks may be due to noise in the assay and not reflect true chromatin accessibility, we calculated an irreproducible discovery rate (IDR)[39] for all pairs of replicates across a cell type. The IDR is an estimate of the threshold where two ranked lists of results, in this case peak calls ranked by P value, no longer represent reproducible events. Using this measure, we excluded peaks that were not reproducible (IDR < 5e-3) across at least one pair of replicates in each mouse or human cell type.

ATAC-Seq atlas creation

Peaks found reproducibly in each mouse cell type were combined to create a genome-wide atlas of accessible chromatin regions. Reproducible peaks from different samples were merged if they overlapped by more than 75%. To create the atlas of accessible peaks for the human samples, reproducible peaks from the normal human cell types (HN, HCM, and HEM) and the tumor-derived cells (PD1hi) were combined. There was greater variation between the human TIL samples than between T cell samples from healthy donors; this led to fewer reproducible peaks being called in the TIL samples. Like the mouse atlas, peaks overlapping by more than 75% were merged in the human atlas. Numbers of called peaks and reproducible peaks for each sample type are listed in Supplementary Data File 1.

Assignment of ATAC-Seq peaks to genes

The RefSeq transcript annotations of the hg38 version of the human genome and the mm10 version of the mouse genome were used to define the genomic location of transcription units. For genes with multiple gene models, the longest transcription unit was used for the gene locus definition. ATAC peaks located in the body of the transcription unit, together with the 2-kb regions upstream of the TSS and downstream of the 3′ end, were assigned to the gene. If a peak was found in the overlap of the transcription units of two genes, one of the genes was chosen arbitrarily. Intergenic peaks were assigned to the gene whose TSS or 3′ end was closest to the peak. In this way, each peak was unambiguously assigned to one gene. Peaks were annotated as promoter peaks if they were within 2kb of a transcription start site. Non-promoter peaks were annotated as intergenic, intronic, or exonic according to the relevant RefSeq transcript annotation.

ATAC-Seq peak atlas summary

We found a total of 75,689 reproducible ATAC-Seq peaks in the mouse samples. Examining genomic locations, 39.6% of the peaks were found in introns, 36.3% were found in intergenic regions, 22.1% were found in promoters and 2.1% were found in exons. In the human samples, we found a total of 42,104 reproducible ATAC-Seq peaks. Among these peaks, 34.0% were found in introns, 29.9% were found in intergenic regions, 34.0% were found in promoters, and 2.0% were found in exons. Chromosome-wide genomic coverage for all (autosomal) chromosomes and all samples was examined and no systemic bias was observed.

Principal Component Analysis

PCA plots were generated using read counts against all mouse or human atlas peaks. These read counts were processed using the variance-stabilizing transformation built into the DESeq2 package[40].

Differential peak accessibility

Reads aligning to atlas peak regions were counted using the summarizeOverlaps function of the R packages GenomicAlignments v1.2.2 and GenomicRanges v1.18.4[41]. Differential accessibility of these peaks was then calculated for all pairwise comparisons of cell types using DESeq2 v1.6.3[40].

Peak heatmaps and genome coverage plots

The ATAC-Seq peak heatmaps were created by pooling the DESeq size-factor normalized read counts per atlas peak across replicates of ATAC-Seq data and binning the region +/− 1kb around the peak summit in 20bp bins. All analysis was performed using the original uncapped read counts. Genome coverage plots were generated for each replicate of ATAC-seq and RNA-seq by calculating genome-wide coverage of aligned reads using the bedtools function genomecov[42]. For ATAC-seq samples, this coverage was calculated after shifting the reads to account for the Tn5-induced bias. The coverage values were then normalized using DESeq2-derived size factors and replicates were combined to create one signal track for each sample type. To improve visibility, bins with read counts greater than the 75th percentile + 1.5*IQR were capped at that value. ATAC-Seq and RNA-Seq coverage plots were generated using the Integrated Genomics Viewer (Broad)[43].

Transcription factor peak assignment

Using MEME's[44] curated CisBP[45] transcription factor binding motif (TFBM) reference, we scanned the mouse ATAC-Seq peak atlas with FIMO[46] to find peaks likely to contain each TFBM ($p < 10^{-4}$). The MEME cisBP reference for direct and inferred motifs for *Mus musculus* was curated by the MEME suite developers as follows: to reduce redundancy, for each transcription factor (TF) a single motif was selected according to the following precedence rules. The direct motif was chosen if there was one, otherwise the inferred motif with the highest DNA binding domain (DBD) similarity (according to CisBP) to a TF in another species with a direct motif was chosen. If there was more than one direct motif or inferred motif with the highest DBD similarity, a motif was chosen according to its provenance (CisBP's "Motif_Type" attribute) in the following order: *ChIP-seq, HocoMoco, DeBoer11, PBM, SELEX, B1H, High-throughput Selex CAGE, PBM:CSA:DIP-chip, ChIP-chip, COMPILED, DNaseI footprinting*. Each motif thus determined was linked to a single TF in the CisBP database, following the same precedence rules. The final reference contained 718 motifs between 6 and 30bp in width (average width 10.7bp). Transcription factors with similar FIMO-predicted target peaks were combined into transcription factor families. Similarity of predicted target peak sets was measured using the Jaccard index (size of intersection / size of union). Transcription factors with Jaccard indices greater than 0.7 were combined for further analyses. Relative transcription factor accessibility was calculated using two one-sided Wilcoxon rank-sign tests comparing the distributions of peak heights for peaks containing FIMO predicted transcription factor binding sites. Peak height was defined as the maximum observed number of reads overlapping at any point in the defined peak region.

Footprinting Analysis

ATAC-seq footprints containing FIMO-predicted TF binding sites (p < 1e-4) were selected. Positive and negative strand ATAC-seq cut sites were counted 100bp up- and down-stream of the center of the motif site in each of the selected peaks. The mean number of ATAC-seq cut sites across matching atlas peaks was then plotted to generate the footprint figures.

Diamond Plots

In these plots, each gene is represented by a stack of diamonds corresponding to that gene's associated accessible chromatin regions. The bottom-most peak in this stack corresponds to the $\log_2$ fold change in expression of the gene. The diamonds are colored according to the accessibility change of their ATAC-seq peak with blue indicating closing and red indicating opening. The color scale was based on the rank-order of the peak accessibility changes. In Extended Data Fig. 6d, the color scale ranges from a $\log_2$ fold change of −3.92 to 4.96 (L14/L7).

Comparison of human and mouse ATAC-Seq atlases

UCSC's liftOver tool[47] was used to convert the mouse ATAC-Seq peak atlas from mm10 coordinates to hg38 coordinates. The converted mouse atlas was then compared to the human atlas and 20,642 mouse peaks were within 100bp of a human peak. We compared the results from the UCSC liftover tool and an alternative method, bnMapper[48] and confirmed that the set of peaks mapped by bnMapper and by the UCSC liftOver tool was nearly identical (57383/75689 by liftOver and 58299/75689 by bnMapper). Additionally, all 57223 peaks mapped to hg38 by both tools were mapped to the same chromosomal positions. The majority of these conserved peaks were found in promoter regions (56.4%), while relatively fewer were found in intergenic (22.4%), intronic (19.6%), and exonic (1.5%) regions. For non-promoter peaks conserved between human and mouse, Spearman correlations of $\log_2$FC were calculated between human N and human EM, CM or PD1^{hi} TIL versus $\log_2$FC between murine N and functional E5, E7, M and dysfunctional L5 to L60.

RNA-Seq

Raw ATAC-Seq reads were trimmed and filtered for quality using Trim Galore! v0.4.0 (http://www.bioinformatics.babraham.ac.uk/projects/trim_galore/), powered by CutAdapt v1.8.1 (http://dx.doi.org/10.14806/ej.17.1.200) and FastQC v0.11.3 (http://www.bioinformatics.babraham.ac.uk/projects/fastqc/). Paired-end reads were aligned using STAR[49] against either mm10 or hg38. The RefSeq transcript annotations of the hg38 version of the human genome and the mm10 version of the mouse genome were used for the genomic location of transcription units. Reads aligning to annotated exon regions were counted using the summarizeOverlaps function of the R packages GenomicAlignments v1.2.2 and GenomicRanges v1.18.4[41]. Differential expression of genes across cell types was calculated using DESeq2 v1.6.3[40]. FDR correction of 0.05 was imposed unless otherwise stated. A $\log_2$fold change cutoff of 1 was used in some analyses as indicated.

Pathway analysis

Enrichment of GO terms in sets of ATAC-Seq peaks was calculated using GREAT (Genomic Regions Enrichment of Annotations Tool) using default parameters[50]. The full ATAC-Seq atlas was used as the background set.

Membrane protein analysis

To identify membrane proteins that distinguished early (L5-L7) from late (L14-L60) dysfunctional TST, RNA-Seq data was analyzed for genes contained within the Gene

Ontology category 0016020 (membrane proteins). The top 50 most up and down-regulated genes (size-factor normalized RPKM) when compared between L5-L7 v L14-L60 were plotted in a heatmap (row-normalized). Protein expression was assessed by flow cytometry for those membrane proteins for which monoclonal antibodies were available. Murine targets (clone; supplier): CD5 (53–7.3; eBioscience), CD30L (RM153; eBioscience), CD38 (90; Biolegend), and CD101 (Moushi101; eBioscience). Human targets: CD5 (L17F12; Biolegend), CD38 (HB7; eBioscience), CD101 (BB27; Biolegend).

Data reporting

No statistical methods were used to predetermine sample size. The investigators were not blinded to allocation during experiments and outcome assessment. Mice or human samples were excluded if donor or tumor-infiltrating CD8 T cells could not be found.

Data availability

All data generated and supporting the findings of this study are available within the paper. The RNA-Seq and ATAC-Seq data have been deposited in the Gene Expression Omnibus [GEO Super-Series accession number GSE89309 (GSE89307 for RNA-Seq, GSE89308 for ATAC-Seq]. Source Data are provided with the online version of the paper. Additional information and materials will be made available upon request.

Extended Data

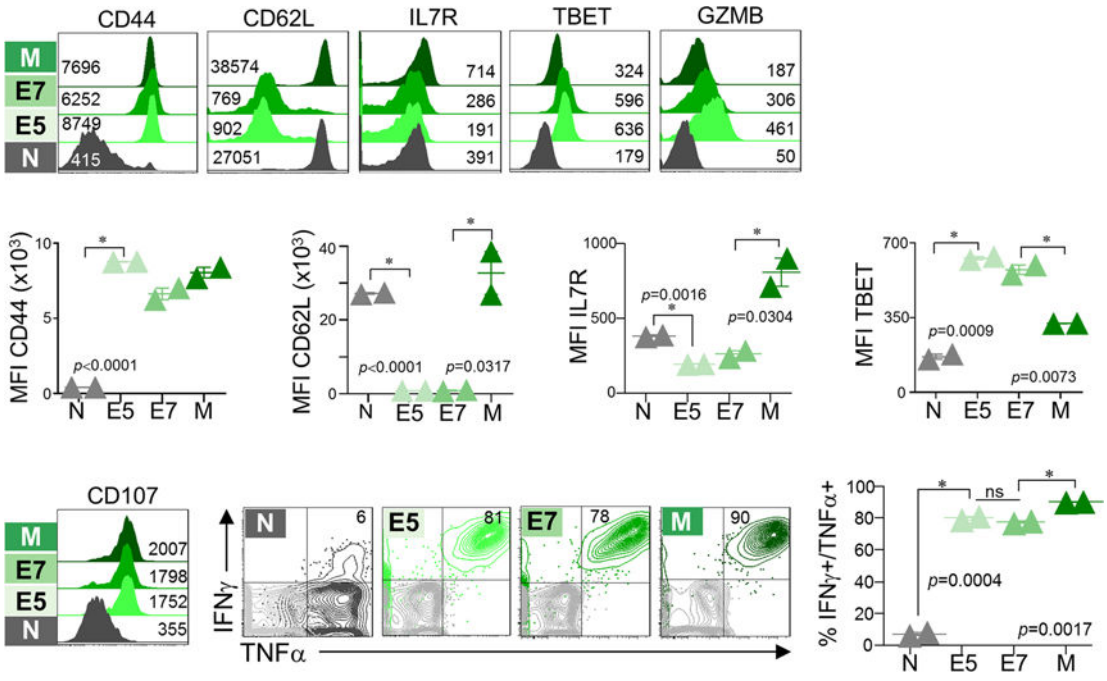

Extended Data Figure 1. Phenotypic and functional characteristics of naïve TCR_{TAG} CD8 T cells differentiating to effector and memory T cells during acute *Listeria* infection

Naïve TCR_{TAG} (N; Thy1.1$^+$) were transferred into B6 (Thy1.2$^+$) mice, which were immunized with *Lm*TAG one day later. At days 5, 7, and 60+ post *Lm*TAG, effector (E5 and E7), and memory (M) T cells were isolated from spleens and assessed for phenotype and

function. Flow cytometric analysis of CD44, CD62L, IL7Rα, TBET, and GZMB expression directly *ex vivo* (upper panel; inset numbers show MFI), and intracellular IFNγ and TNFα production and CD107 expression after 4-hour *ex vivo* TAG peptide stimulation (lower panel). Flow plots are gated on $CD8^+$ $Thy1.1^+$ cells. For cytokine production, in grey are shown no-peptide control cells. (n=8 total, with n=2 per cell state). Each symbol represents an individual mouse. Data show mean ± s.e.m; *P* values calculated using unpaired, two-tailed Student's t-test. Data are representative of more than 4 independent experiments.

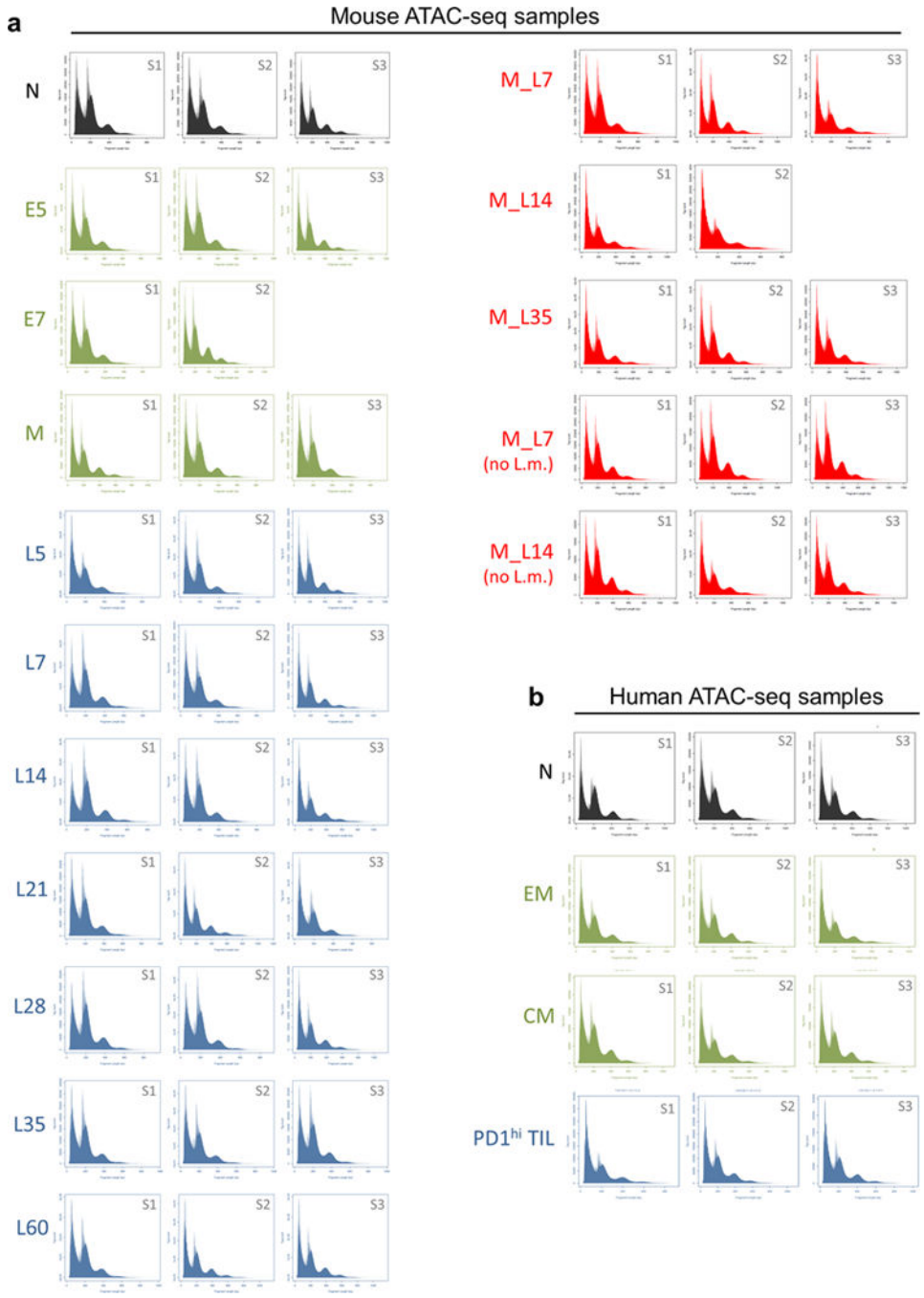

Extended Data Figure 2. Fragment length distribution plots of ATAC-seq samples

Plots are shown for all mouse (a) and human (b) CD8 T cell ATAC-seq samples displaying fragment length (bp; x-axis) and read counts (y-axis). (S1, S2, S3 = replicates per sample group).

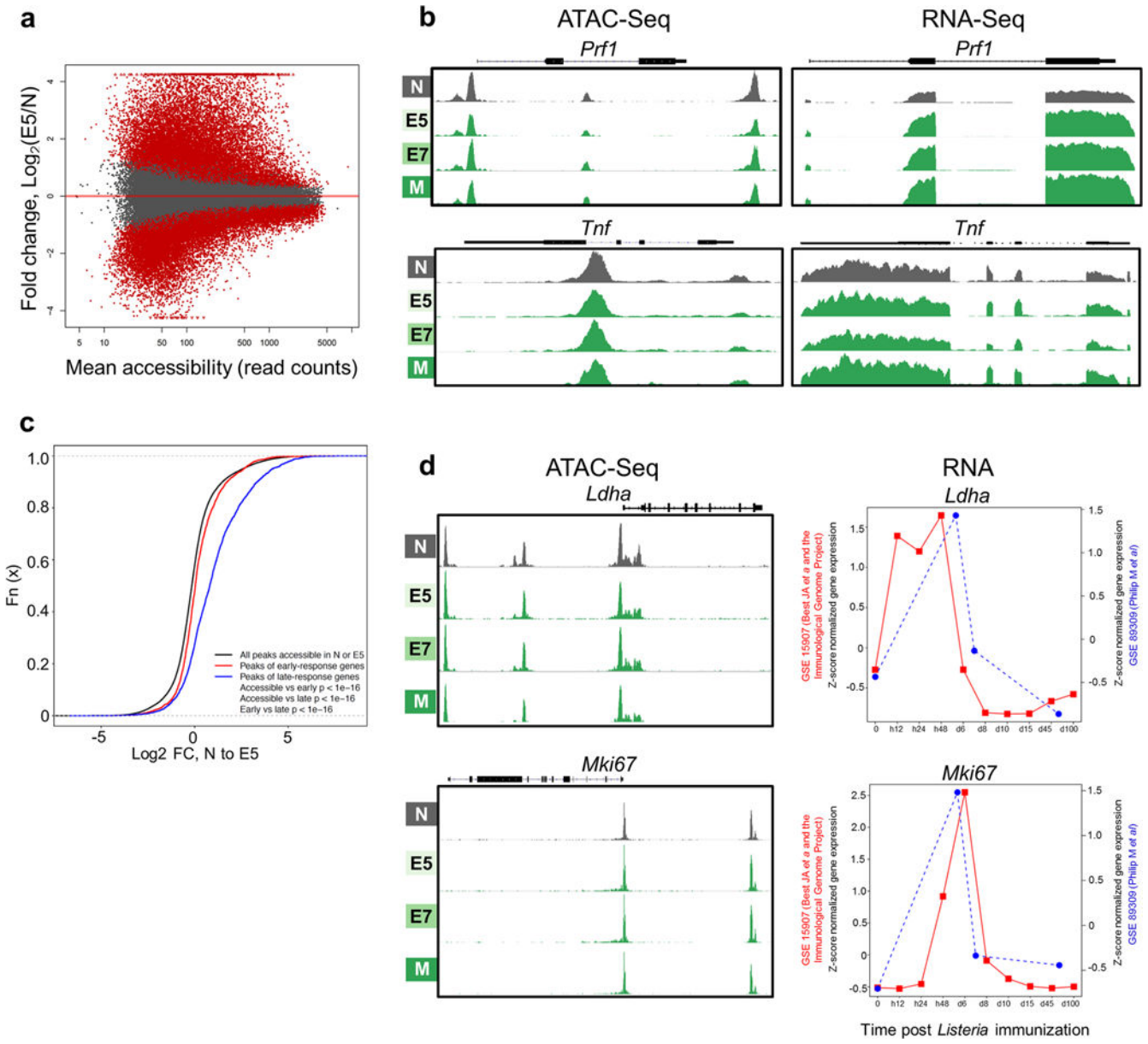

Extended Data Figure 3. Epigenetic and transcriptional regulation of normal CD8 differentiation

a, ATAC-Seq data reveals massive chromatin remodeling during normal CD8 T cell differentiation. MA plot of Naïve (N) and Day 5 Effectors (E5) showing $\log_2$ ratios of peak accessibility (E5/N) versus mean read counts for all atlas peaks. Significantly differentially accessible peaks are shown in red (*FDR* < 0.05). **b**, Epigenetic and transcriptional regulation of CD8 effector genes. ATAC-seq (left) and RNA-seq (right) signal profiles of *Prf1* and *Tnf* in Naïve (N), Effectors (E5 and E7), and Memory (M) TCR_{TAG} during acute *Lm*TAG

infection. **(c – d)**, Epigenetic and transcriptional regulation of early CD8 response genes in TCR_{TAG} during acute listeria infection. Published expression data from the Immunological Genome Project (JA Best et al, *Nat Imm* (2013); GSE 15907) were used; early-response genes increase in expression within the first 12–24 hours and late-response genes increase expression 24–48 hours after naïve T cells encounter *Lm*OVA as determined by Best JA *et al.* **c**, Cumulative distribution function of peak accessibility changes between N and E5. Peaks associated with early-response genes show fewer changes in accessibility as compared to peaks associated with late-response genes. The black line shows all peaks accessible in N or E5, the red line shows peaks associated with early-response genes and the blue line shows peaks associated with late-response genes. **d**, ATAC-seq signal profiles (left) and RNA expression (right) of the early response genes *Ldha* (top) and *Mki67* (bottom) in N, E5/E7, and M TCR_{TAG} during acute *Lm*TAG infection (blue line; GSE 89309; current dataset Philip M *et al.*) overlaid with expression data from Best JA *et al.*/Immunological Genome Project (red line).

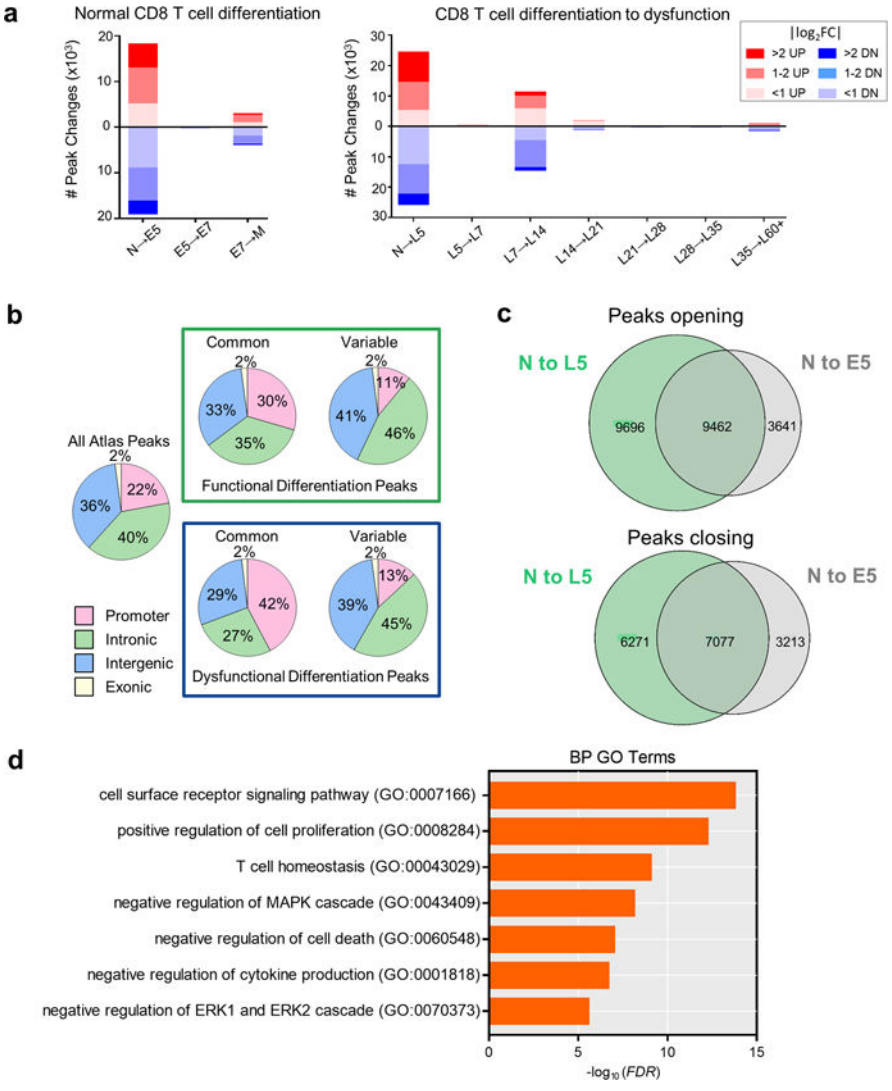

Extended Data Figure 4. Chromatin peak accessibility changes during normal and dysfunctional CD8 T cell differentiation

a, Number of DESeq-determined chromatin peak accessibility changes during each transition during normal CD8 T cell differentiation (*Listeria* infection) (right) and CD8 T cell differentiation to dysfunction during tumorigenesis (left) broken down by $|\log_2 FC|>2$, $|\log_2 FC|=1–2$, and $|\log_2 FC|<1$. **b**, Chromatin accessibility peaks gained or lost during normal and dysfunctional CD8 T cell differentiation were mainly found in intergenic and intronic regions. Pie charts showing the proportions of reproducible ATAC-seq peaks in exonic, intronic, intergenic and promoter regions. (Left) Distribution for all peaks in the atlas. Green box – normal CD8 T cell differentiation during *Lm*TAG immunization; distribution for common and variably accessible peaks in N, E5, E7, and M functional CD8 T cells. Blue box – differentiation to dysfunction in progressing tumors; distribution for common and variably accessible peaks in N, L5, L7, L14, L21, L28, L35, and L60+. Variable = significant change in at least one cell type comparison (*FDR*<0.05, $|\log_2 FC|>1$). Common = no change in any cell type comparison. **c**, Venn diagrams show the number of significantly-changed peaks during the transition from Naive (N) to D5-effectors (E5) TCR_{TAG} during acute listeria *Lm*TAG infection versus N to L5 early malignant lesion-infiltrating TCR_{TAG} (*FDR*< 0.05, $|\log_2 FC|>2$) (Upper) Venn diagram shows opening peaks; (lower) Venn diagram shows closing peaks. **d**, Selected Biological process (BP) Gene Ontology (GO) terms enriched in peaks open in L5 relative to E5 as determined through GREAT analysis.

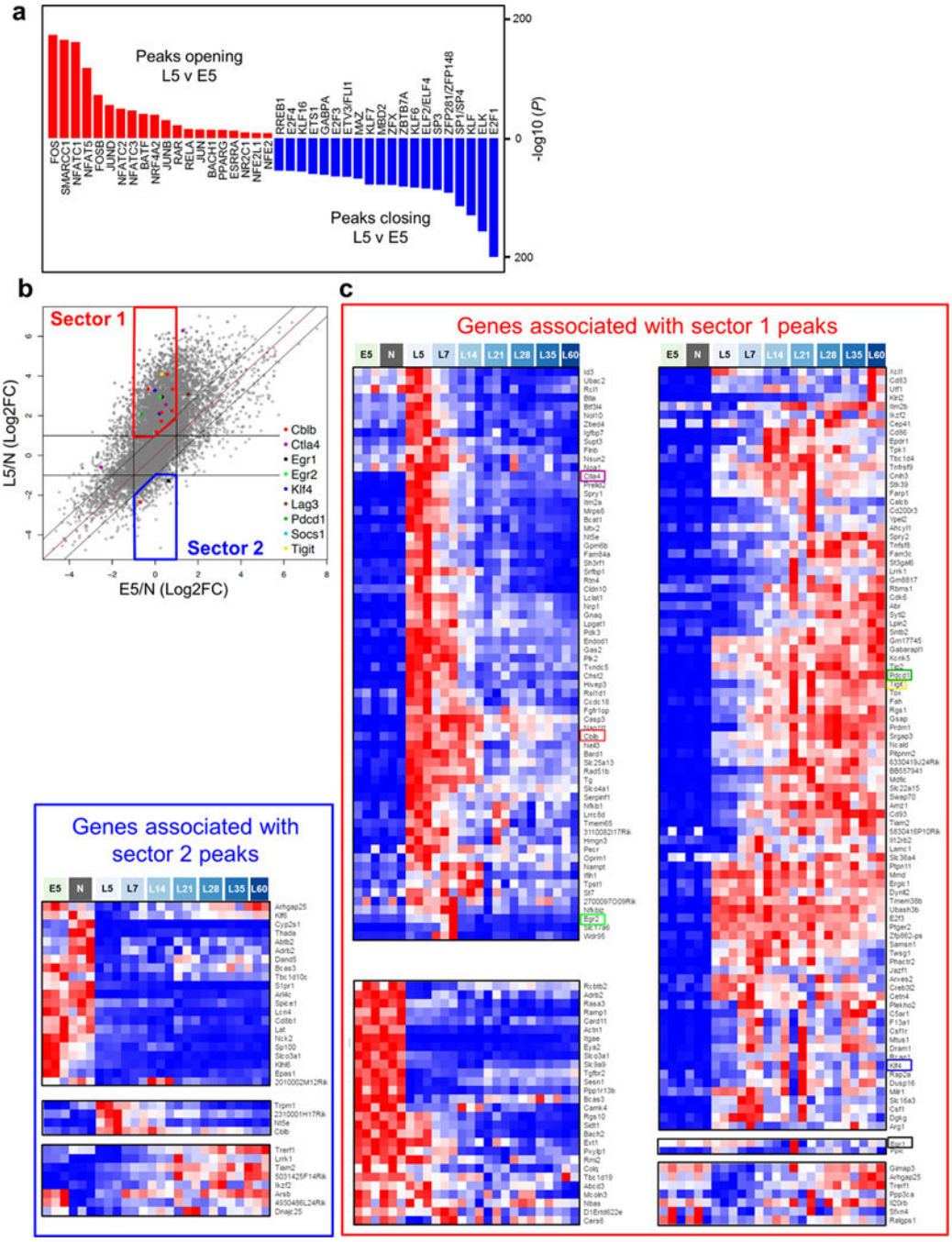

Extended Data Figure 5. NFATC1 targets become significantly more accessible during differentiation to dysfunction in early malignant lesions as compared to normal effector differentiation

a, Top 20 most-significantly enriched TF motifs in peaks opening (red) and closing (blue) between L5 and E5. **b**, Scatterplot comparing the changes in peak accessibility for all differentially-accessible peaks containing the NFATC1 motif during the transition from Naive (N) to D5-Effectors (E5) TCR_{TAG} during acute listeria *Lm*TAG infection versus N to L5 in pre-malignant lesions (*FDR*< 0.05, $|\log_2 FC|>1$). Highlighted are NFATC1 target peaks associated with genes encoding negative regulatory transcription factors and inhibitory

receptors. Some genes, e.g. *Cblb* and *Klf4*, had multiple NFATC1 target peaks, including peaks that decreased in accessibility. **c**, Genes with more accessible NFATC1 target peaks during differentiation to dysfunction in malignant lesions show increased expression levels. Gene expression for genes with peaks in sector 1 and sector 2, with increased and decreased accessibility in L5 vs E5 respectively. Heatmaps show RNA-Seq expression data (row-normalized) for differentially-expressed ($P < 0.01$, $|\log2FC| > 1$) genes with NFATC1 target peaks contained in Sector 1 (red box) or Sector 2 (blue box) of scatterplot presented **b**. The majority of Sector 1 genes (195/223, 87%) revealed increased expression in dysfunctional TST as compared to E5, while the majority of Sector 2 genes (21/33, 63%) had decreased expression. Genes are clustered by row according to expression across the samples. Interestingly, while many genes in Sector 1 had transiently increased expression in L5 and L7 (red box, upper left), many genes increased in expression at later stages of tumorigenesis at L14 and beyond (red box, upper right). This suggests that NFATC1 activation of downstream targets (negative regulators of T cell function) may not only induce early dysfunction, but may cause or contribute to the transition from plastic to fixed dysfunction.

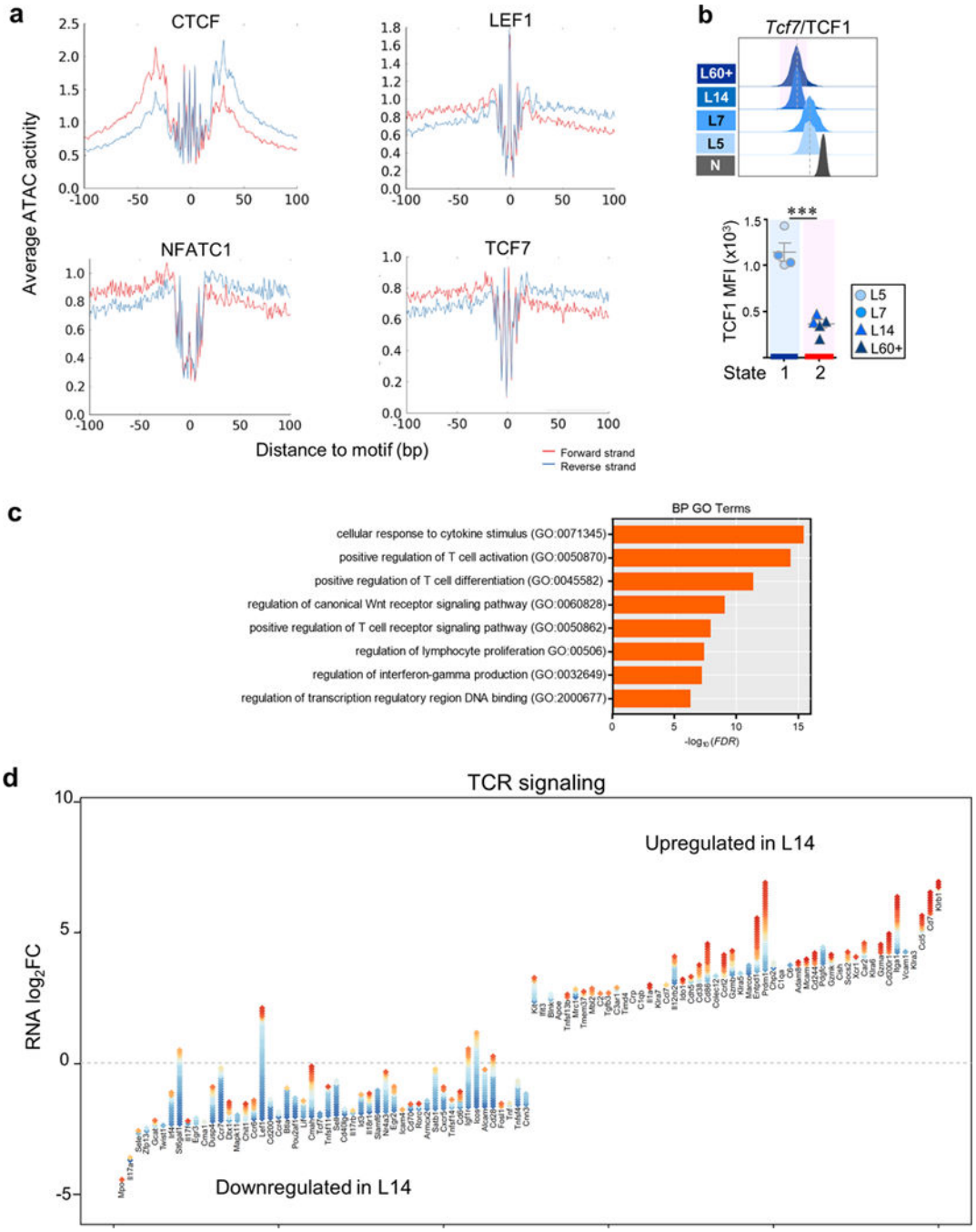

Extended Data Figure 6. Epigenetic and transcriptional changes during the L7 to L14 transition

a, Transcription factor footprinting in chromatin accessible regions. ATAC cut site distributions show footprints for CTCF, LEF1, NFATC1, and TCF7 in naïve CD8 T cells. Shown is the mean number of ATAC cut sites on the forward (red) or reverse (blue) strand 100bp up and downstream of the TF motif site, calculated for atlas peaks predicted by FIMO to be bound by the respective TF ($p<10^{-4}$). **b**, TCF1 expression (MFI; mean fluorescence intensity). Each symbol represents individual mouse. Mean ± s.e.m. shown; *** $P \leq 0.0001$ (Student's *t*-test). **c**, Selected Biological Processes (BP) (Gene Ontology [GO] terms)

enriched in genes which significantly lost chromatin accessibility during the L7 to L14 transition as determined through GREAT analysis. **d**, Gain and losses of regulatory elements for top 50 most differentially expressed genes associated with TCR signaling during the L7 to L14 transition. Top 25 genes associated with TCR signaling with highest and lowest logFC gene expression changes are shown. Each gene is illustrated by a stack of diamonds, where each diamond represents a chromatin peak associated with the gene. Red diamonds denote peaks gained in the transition, blue diamonds denote peaks that were lost.

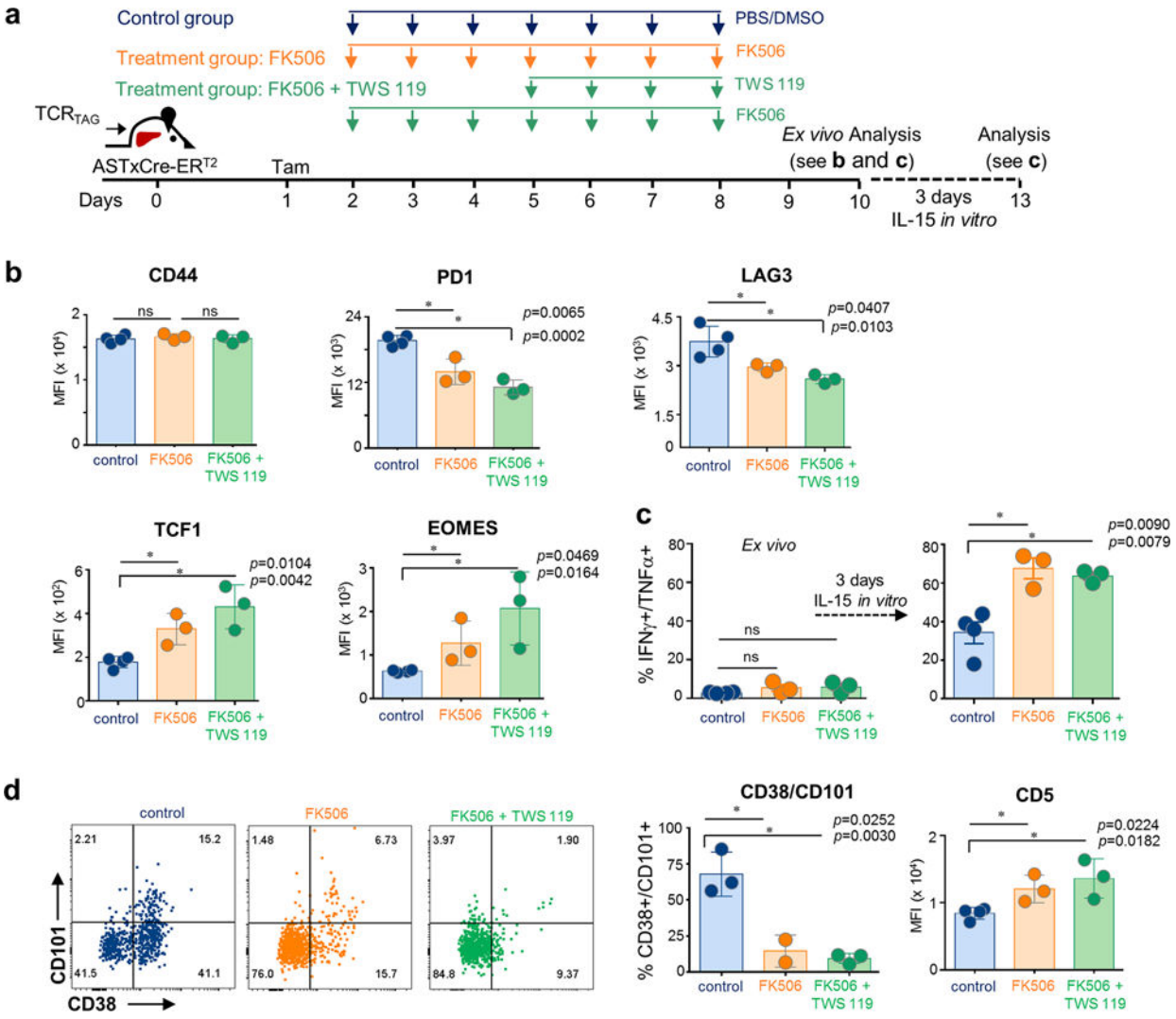

Extended Data Figure 7. Pharmacological targeting of NFAT and Wnt/β-catenin signaling prevents TST differentiation to the fixed dysfunctional state *in vivo*

a, Experimental scheme. Naïve TCR_{TAG} ($Thy1.1^+$) were transferred into ASTxCre-ER^{T2} ($Thy1.2^+$) mice which were treated with tamoxifen (Tam) one day later. At days 2–9 mice were treated with the calcineurin inhibitor FK506 (2.5mg/kg/mouse) alone (FK506 treatment group; orange), or in combination with the GSK3β inhibitor TWS119 (0.75mg/mouse; days 5–8) (FK506 + TWS119 treatment group; green), or PBS/DMSO (control group; blue) as indicated. At day 10, TCR_{TAG} were isolated from livers and assessed for

phenotype and function. **b**, Flow cytometric analysis of CD44, PD1, LAG3, TCF1, and EOMES expression of TCR_{TAG}. **c**, IFNγ and TNFα production of TCR_{TAG} isolated at day 10 (left panel; straight *ex vivo*), and post 3 days IL15 *in vitro* culture (right panel). Each symbol represents an individual mouse. Data show mean ± s.e.m; *P* values calculated using unpaired two-tailed t-test. **d**, Representative flow cytometric analysis of CD38 and CD101 expression of TCR_{TAG} (numbers indicate %); CD38, CD101 and CD5 expression. Each symbol represents an individual mouse. Data show mean ± s.e.m; *P* values calculated using unpaired two-tailed t-test. These data are representative of 2 independent experiments (with total n=10 for Exp#1; n=9, Exp#2).

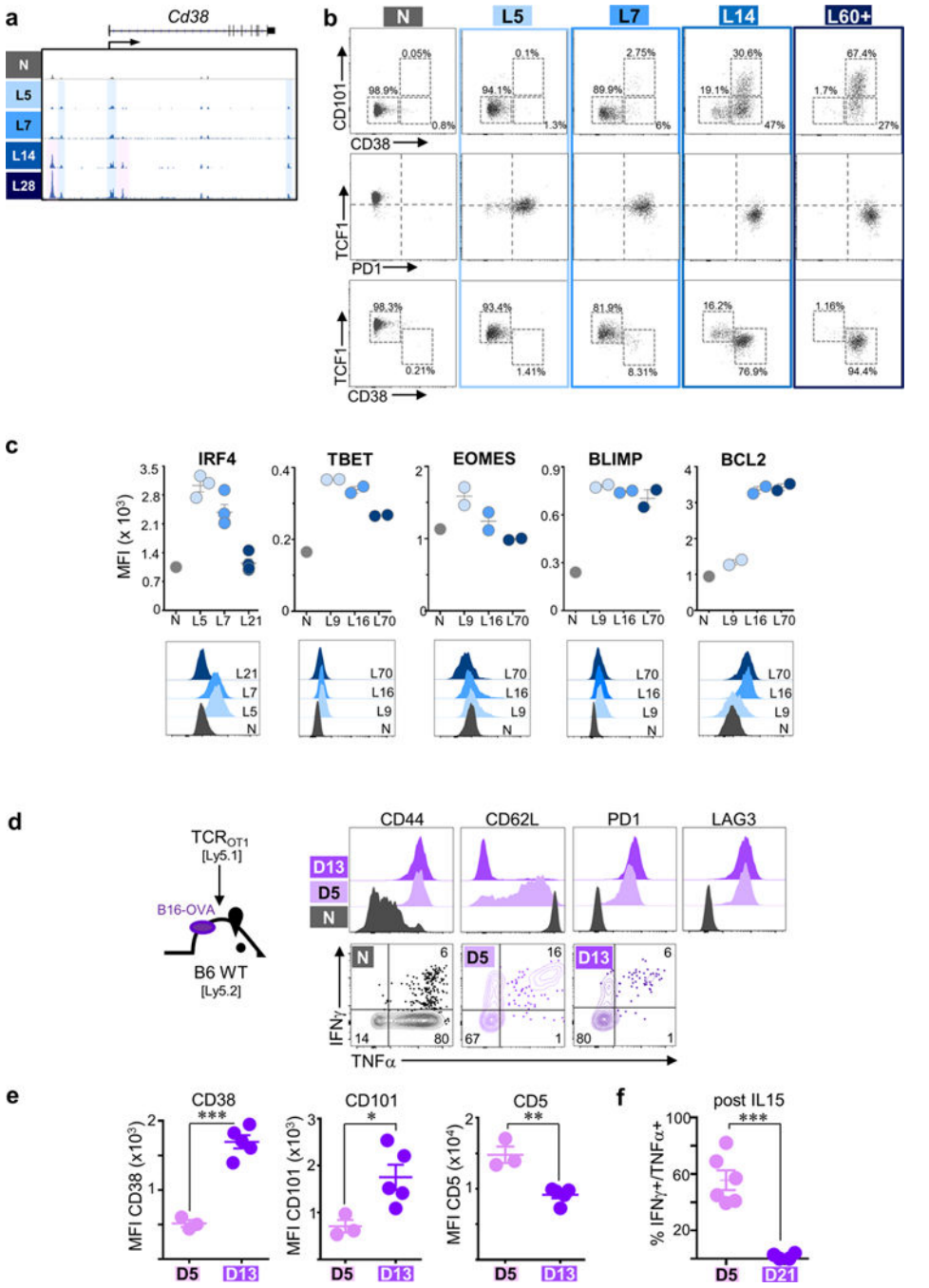

Extended Data Figure 8. Epigenetic and expression dynamics of membrane proteins and transcription factors associated with T cell dysfunction

a, ATAC-Seq signal profile across the *Cd38* loci with "state 2" uniquely accessible peaks highlighted in pink; activation-associated peaks highlighted in blue. **b**, Expression profiles of N, L5, L7, L14, and L60+ TCR_{TAG} for CD101 versus CD38, TCF versus PD1, and TCF1 versus CD38 by flow cytometric analysis. **c**, Expression of transcription factors and other proteins on tumor-specific TCR_{TAG} T cells over the course of tumorigenesis (MFI; mean fluorescence intensity). Each symbol represents an individual mouse. Data shows mean ±

s.e.m. (bottom panel). Representative flow histogram overlays are shown. **(d – f)** TCR_{OT1} TST in established B16-OVA tumors enter plastic and fixed dysfunctional states. **d**, Immunophenotype and cytokine production of TCR_{OT1} re-isolated from established B16-OVA tumors 5 (D5) and 13 (D13) days post transfer. **e**, CD38, CD101 and CD5 expression on D5 and D13 TCR_{OT-1}. **f**, Cytokine production of D5 and D21 TCR_{OT-1} after 3 days IL-15 *in vitro* culture. Each symbol represents individual mouse. Mean ± s.e.m. shown; **P*=0.03, ***P*=0.002, ****P*≤0.0003 (Student's *t*-test).

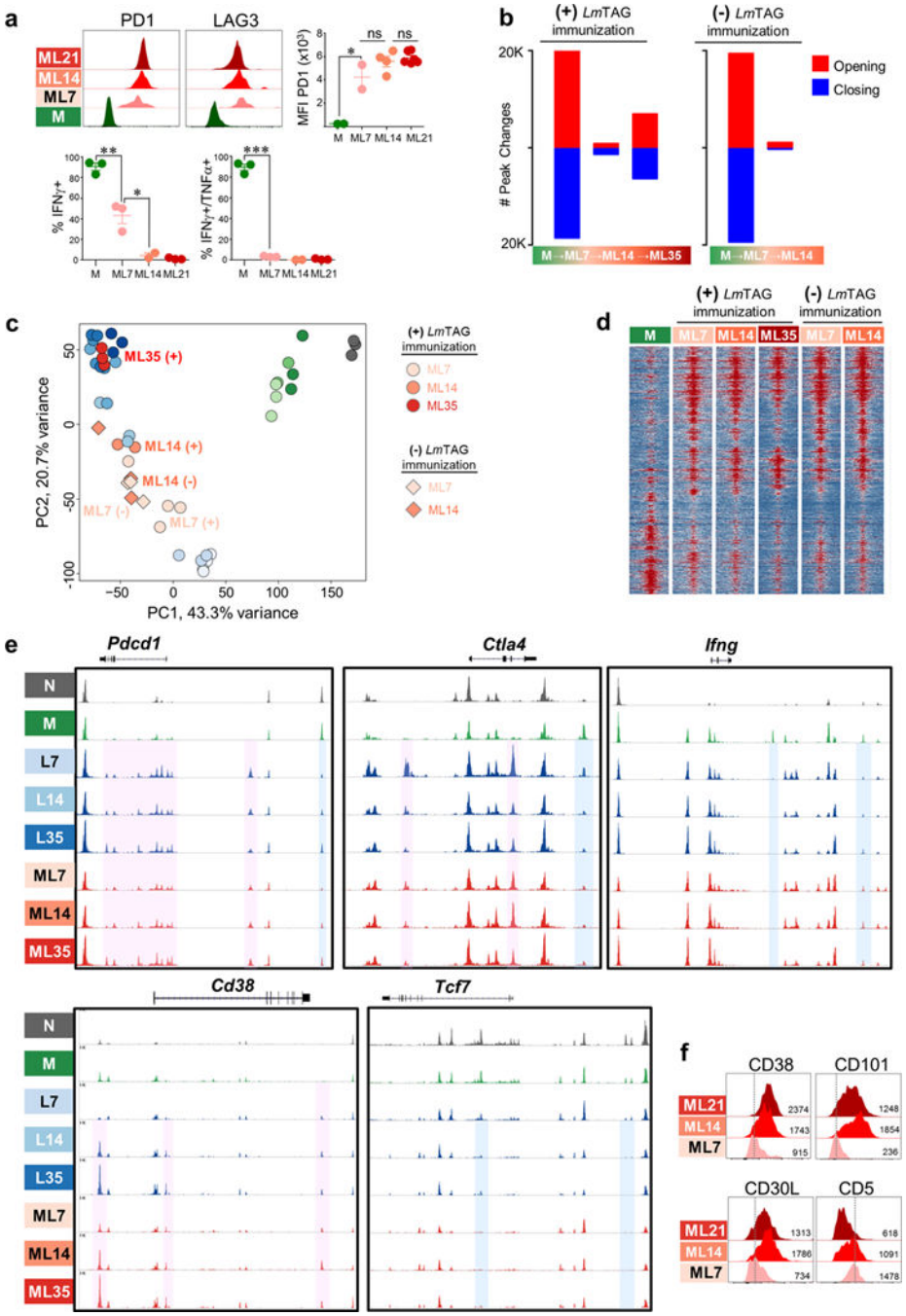

Extended Data Figure 9. Chromatin state dynamics of memory TCR_{TAG} differentiating to the dysfunctional state in solid tumors

a, PD1 and LAG3 expression and cytokine production of memory TCR_{TAG} in liver tumors. Each symbol represents individual mouse. Mean ± s.e.m. shown; **P*=0.03, ***P*=0.006, ****P*<0.0001 (Student's *t*-test); representative of 4 independent experiments. **b**, Numbers of ATAC-seq peaks significantly opening or closing (*FDR* < 0.05) during each transition as memory TCR_{TAG} differentiate to the dysfunctional state 7, 14, and 35 days post transfer into HCC-tumor bearing ASTxAlb:Cre mice with [(+); left] and without [(-); right] listeria *Lm*TAG immunization; peaks opening (red), peaks closing (blue). **c**, Principal component analysis of peak accessibility during naïve TCR_{TAG} differentiation in acute infection (green), early tumorigenesis (blue), and memory TCR_{TAG} in established HCC (red). Circles = with *Lm*TAG immunization; diamonds = no *Lm*TAg immunization. **d**, Chromatin accessibility heatmap. Each row represents one of 11,698 selected peaks (differentially accessible between any sequential cell comparison; *FDR* <0.05, $|\log_2 FC|>2$). Shown are +/− 1kb from the peak summit (2kb total per region). **e**, ATAC-seq signal profiles of *Pdcd1*, *Ctla4*, *Cd38, Tcf7*, and *Ifng* genes of Naïve (N; grey), Memory (M; green), L7, L14, L35 (blue series), and ML7, ML14, and ML35 (red series) TCR_{TAG}. Pink boxes highlight peaks that become accessible in dysfunctional T cells compared to Naïve and Memory; blue boxes highlight peaks that become inaccessible in dysfunctional TCR_{TAG} compared to Naïve and Memory TCR_{TAG}. **f**, CD38, CD101, CD30L, and CD5 expression on ML7, ML14, ML21. Inset numbers show MFI.

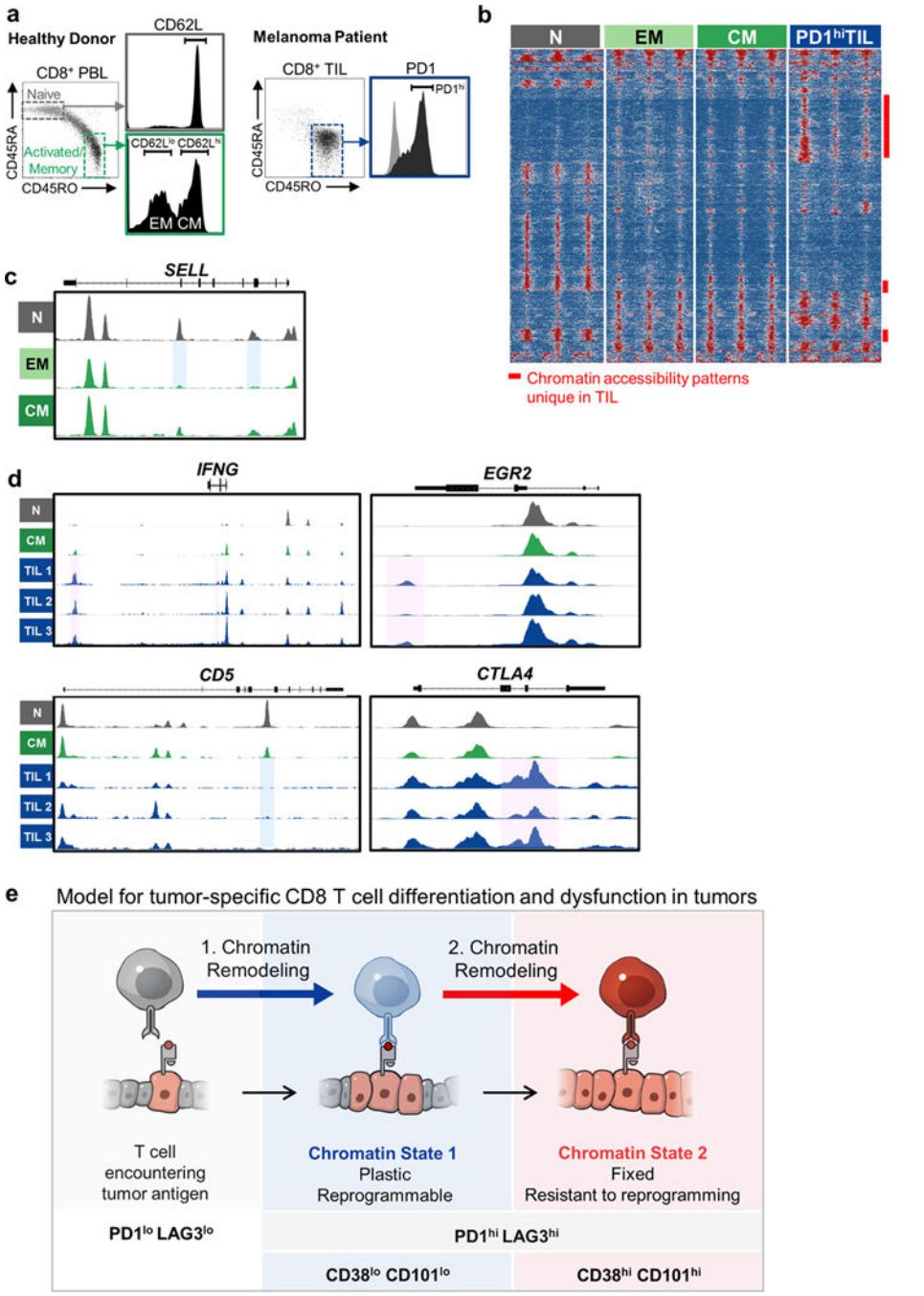

Extended Data Figure 10. Chromatin states of human PD1^{hi} tumor-infiltrating CD8+ T cells and model for CD8 TST differentiation and dysfunction in tumors

a, Sorting scheme of peripheral blood lymphocytes for Naïve (N), Effector Memory (EM), Central Memory (CM) CD8 T cell populations (left), and PD1hi CD8 TIL from melanoma and NSCLC patients. **b**, Differentially accessible ATAC-seq peaks grouped by DESeq-defined differential accessibility pattern. Each column represents one biological replicate. Samples shown include CD45RA+ CD45RO- (Naïve; N; grey), CD45RA- CD45RO+, CD62L- (Effector Memory; EM; light green) and CD45RA- CD45RO+, CD62L+ (Central

Memory; CM; dark green) peripheral blood $CD8^+$ T cells from healthy donors, and CD45RA- CD45RO+, $PD1^{hi}$ CD8+ T cells isolated and flow-sorted from human melanoma and lung tumors ($PD1^{hi}$ TIL; blue). Open, accessible chromatin regions are presented in red; inaccessible chromatin regions are presented in blue. **c**, ATAC-seq signal profiles of *SELL* in N, EM and CM. Blue boxes highlight peaks that remain accessible in CM or become inaccessible in EM compared to N respectively. **d**, ATAC-seq signal profiles of *IFNG, EGR2, CD5, CTLA4*. Pink and blue boxes highlight peaks that become accessible or inaccessible in $PD1^{hi}$ TIL compared to N or CM respectively. **e**, Model for tumor-specific CD8 T cell differentiation and dysfunction in tumors.

Supplementary Material

Refer to Web version on PubMed Central for supplementary material.

Acknowledgments

We thank Joris van der Veeken, Varintra Krisnawan, Yuri Pritykin, and Billel Gasmi for helpful discussions and technical support; Steve Reiner for helpful discussions; and the MSKCC Flow Cytometry Core. T.M., M.H., J.D.W., A.S. are members of the Parker Institute for Cancer Immunotherapy. This work was supported by NIH-NCI grants R00 CA172371 (to A.S.), K08 CA158069 (to M.P.), and U54 CA209975 (to C.S.L and A.S.), NHGRI grant U01 HG007893 (to C.S.L.), V Foundation for Cancer Research (to A.S.), the William and Ella Owens Medical Research Foundation (to A.S.), the *Josie Robertson Young Investigator* Award (to A.S.), and the MSKCC Core Grant P30 CA008748. The Integrated Genomics Operation Core was supported by Cycle for Survival and the Marie-Josée and Henry R. Kravis Center for Molecular Oncology.

References

1. Hellstrom I, Hellstrom KE, Pierce GE, Yang JP. Cellular and humoral immunity to different types of human neoplasms. Nature. 1968; 220:1352–1354. [PubMed: 4302696]
2. Khalil DN, Smith EL, Brentjens RJ, Wolchok JD. The future of cancer treatment: immunomodulation, CARs and combination immunotherapy. Nat Rev Clin Oncol. 2016; 13:273–290. [PubMed: 26977780]
3. Snyder A, et al. Genetic basis for clinical response to CTLA-4 blockade in melanoma. The New England journal of medicine. 2014; 371:2189–2199. [PubMed: 25409260]
4. Kelderman S, Schumacher TN, Haanen JB. Acquired and intrinsic resistance in cancer immunotherapy. Mol Oncol. 2014; 8:1132–1139. [PubMed: 25106088]
5. Rizvi NA, et al. Cancer immunology. Mutational landscape determines sensitivity to PD-1 blockade in non-small cell lung cancer. Science. 2015; 348:124–128. [PubMed: 25765070]
6. Schietinger A, et al. Tumor-Specific T Cell Dysfunction Is a Dynamic Antigen-Driven Differentiation Program Initiated Early during Tumorigenesis. Immunity. 2016; 45:389–401. [PubMed: 27521269]
7. Zhang JA, Mortazavi A, Williams BA, Wold BJ, Rothenberg EV. Dynamic transformations of genome-wide epigenetic marking and transcriptional control establish T cell identity. Cell. 2012; 149:467–482. [PubMed: 22500808]
8. Scharer CD, Barwick BG, Youngblood BA, Ahmed R, Boss JM. Global DNA methylation remodeling accompanies CD8 T cell effector function. J Immunol. 2013; 191:3419–3429. [PubMed: 23956425]
9. Russ BE, et al. Distinct epigenetic signatures delineate transcriptional programs during virus-specific CD8(+) T cell differentiation. Immunity. 2014; 41:853–865. [PubMed: 25517617]
10. Shih HY, et al. Developmental Acquisition of Regulomes Underlies Innate Lymphoid Cell Functionality. Cell. 2016; 165:1120–1133. [PubMed: 27156451]

11. Buenrostro JD, Giresi PG, Zaba LC, Chang HY, Greenleaf WJ. Transposition of native chromatin for fast and sensitive epigenomic profiling of open chromatin, DNA-binding proteins and nucleosome position. Nat Methods. 2013; 10:1213–1218. [PubMed: 24097267]
12. Staveley-O'Carroll K, et al. In vivo ligation of CD40 enhances priming against the endogenous tumor antigen and promotes CD8+ T cell effector function in SV40 T antigen transgenic mice. J Immunol. 2003; 171:697–707. [PubMed: 12847236]
13. Brockstedt DG, et al. Listeria-based cancer vaccines that segregate immunogenicity from toxicity. Proc Natl Acad Sci U S A. 2004; 101:13832–13837. [PubMed: 15365184]
14. Anders S, Huber W. Differential expression analysis for sequence count data. Genome Biol. 2010; 11:R106. [PubMed: 20979621]
15. Araki Y, Fann M, Wersto R, Weng NP. Histone acetylation facilitates rapid and robust memory CD8 T cell response through differential expression of effector molecules (eomesodermin and its targets: perforin and granzyme B). J Immunol. 2008; 180:8102–8108. [PubMed: 18523274]
16. Denton AE, Russ BE, Doherty PC, Rao S, Turner SJ. Differentiation-dependent functional and epigenetic landscapes for cytokine genes in virus-specific CD8+ T cells. Proc Natl Acad Sci U S A. 2011; 108:15306–15311. [PubMed: 21876173]
17. Best JA, et al. Transcriptional insights into the CD8(+) T cell response to infection and memory T cell formation. Nat Immunol. 2013; 14:404–412. [PubMed: 23396170]
18. Peng M, et al. Aerobic glycolysis promotes T helper 1 cell differentiation through an epigenetic mechanism. Science. 2016; 354:481–484. [PubMed: 27708054]
19. Cuylen S, et al. Ki-67 acts as a biological surfactant to disperse mitotic chromosomes. Nature. 2016; 535:308–312. [PubMed: 27362226]
20. Kaech SM, Cui W. Transcriptional control of effector and memory CD8+ T cell differentiation. Nat Rev Immunol. 2012; 12:749–761. [PubMed: 23080391]
21. Sen DR, et al. The epigenetic landscape of T cell exhaustion. Science. 2016; 354:1165–1169. [PubMed: 27789799]
22. Pauken KE, et al. Epigenetic stability of exhausted T cells limits durability of reinvigoration by PD-1 blockade. Science. 2016; 354:1160–1165. [PubMed: 27789795]
23. Scott-Browne JP, et al. Dynamic Changes in Chromatin Accessibility Occur in CD8+ T Cells Responding to Viral Infection. Immunity. 2016; 45:1327–1340. [PubMed: 27939672]
24. Macian F. NFAT proteins: key regulators of T-cell development and function. Nat Rev Immunol. 2005; 5:472–484. [PubMed: 15928679]
25. Martinez GJ, et al. The transcription factor NFAT promotes exhaustion of activated CD8(+) T cells. Immunity. 2015; 42:265–278. [PubMed: 25680272]
26. Teague RM, et al. Interleukin-15 rescues tolerant CD8+ T cells for use in adoptive immunotherapy of established tumors. Nat Med. 2006; 12:335–341. [PubMed: 16474399]
27. Li Y, et al. MART-1-specific melanoma tumor-infiltrating lymphocytes maintaining CD28 expression have improved survival and expansion capability following antigenic restimulation in vitro. J Immunol. 2010; 184:452–465. [PubMed: 19949105]
28. Flanagan WM, Corthesy B, Bram RJ, Crabtree GR. Nuclear association of a T-cell transcription factor blocked by FK-506 and cyclosporin A. Nature. 1991; 352:803–807. [PubMed: 1715516]
29. Jain J, et al. The T-cell transcription factor NFATp is a substrate for calcineurin and interacts with Fos and Jun. Nature. 1993; 365:352–355. [PubMed: 8397339]
30. Gattinoni L, et al. Wnt signaling arrests effector T cell differentiation and generates CD8+ memory stem cells. Nat Med. 2009; 15:808–813. [PubMed: 19525962]
31. Schietinger A, Delrow JJ, Basom RS, Blattman JN, Greenberg PD. Rescued tolerant CD8 T cells are preprogrammed to reestablish the tolerant state. Science. 2012; 335:723–727. [PubMed: 22267581]
32. Waugh KA, et al. Molecular Profile of Tumor-Specific CD8+ T Cell Hypofunction in a Transplantable Murine Cancer Model. J Immunol. 2016; 197:1477–1488. [PubMed: 27371726]

METHODS REFERENCES

33. Stahl S, et al. Tumor agonist peptides break tolerance and elicit effective CTL responses in an inducible mouse model of hepatocellular carcinoma. Immunol Lett. 2009; 123:31–37. [PubMed: 19428549]
34. Sinnathamby G, et al. Priming and activation of human ovarian and breast cancer-specific CD8+ T cells by polyvalent Listeria monocytogenes-based vaccines. J Immunother. 2009; 32:856–869. [PubMed: 19752748]
35. Engels B, et al. Relapse or eradication of cancer is predicted by peptide-major histocompatibility complex affinity. Cancer Cell. 2013; 23:516–526. [PubMed: 23597565]
36. Langmead B, Salzberg SL. Fast gapped-read alignment with Bowtie 2. Nat Methods. 2012; 9:357–359. [PubMed: 22388286]
37. Adey A, et al. Rapid, low-input, low-bias construction of shotgun fragment libraries by high-density in vitro transposition. Genome Biol. 2010; 11:R119. [PubMed: 21143862]
38. Zhang Y, et al. Model-based analysis of ChIP-Seq (MACS). Genome biology. 2008; 9:R137. [PubMed: 18798982]
39. Zigler CM, Belin TR. The Potential for Bias in Principal Causal Effect Estimation When Treatment Received Depends on a Key Covariate. Ann Appl Stat. 2011; 5:1876–1892. [PubMed: 22308190]
40. Love MI, Huber W, Anders S. Moderated estimation of fold change and dispersion for RNA-seq data with DESeq2. Genome biology. 2014; 15:550. [PubMed: 25516281]
41. Lawrence M, et al. Software for computing and annotating genomic ranges. PLoS Comput Biol. 2013; 9:e1003118. [PubMed: 23950696]
42. Quinlan AR, Hall IM. BEDTools: a flexible suite of utilities for comparing genomic features. Bioinformatics. 2010; 26:841–842. [PubMed: 20110278]
43. Robinson JT, et al. Integrative genomics viewer. Nat Biotechnol. 2011; 29:24–26. [PubMed: 21221095]
44. Bailey TL, et al. MEME SUITE: tools for motif discovery and searching. Nucleic Acids Res. 2009; 37:W202–208. [PubMed: 19458158]
45. Weirauch MT, et al. Determination and inference of eukaryotic transcription factor sequence specificity. Cell. 2014; 158:1431–1443. [PubMed: 25215497]
46. Grant CE, Bailey TL, Noble WS. FIMO: scanning for occurrences of a given motif. Bioinformatics. 2011; 27:1017–1018. [PubMed: 21330290]
47. Hinrichs AS, et al. The UCSC Genome Browser Database: update 2006. Nucleic Acids Res. 2006; 34:D590–598. [PubMed: 16381938]
48. Denas O, et al. Genome-wide comparative analysis reveals human-mouse regulatory landscape and evolution. BMC Genomics. 2015; 16:87. [PubMed: 25765714]
49. Dobin A, et al. STAR: ultrafast universal RNA-seq aligner. Bioinformatics. 2013; 29:15–21. [PubMed: 23104886]
50. McLean CY, et al. GREAT improves functional interpretation of cis-regulatory regions. Nat Biotechnol. 2010; 28:495–501. [PubMed: 20436461]

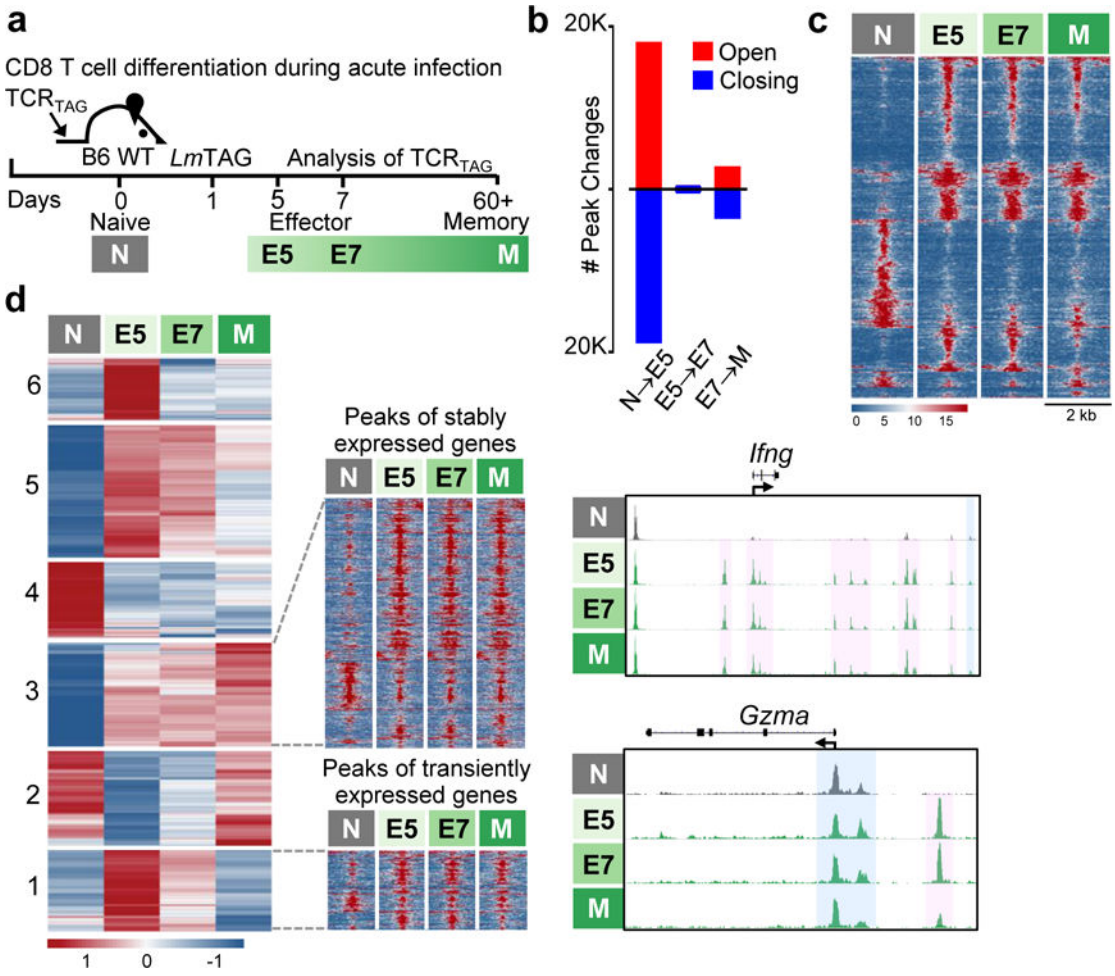

Figure 1. CD8 T cell chromatin state dynamics during acute infection

a, Experimental scheme. **b**, Number of chromatin peak accessibility changes during each transition (*FDR*<0.05). **c**, Chromatin accessibility heatmap grouped by differential accessibility patterns. Each row represents one of 8654 selected peaks (differentially accessible between at least one sequential cell comparison; *FDR* <0.05, $|\log_2 FC|>2$). **d**, (Left) K-means clustered (K = 6, row-normalized) RNA-Seq data for 1758 differentially expressed genes ($|\log_2 FC|>1$, *FDR*<0.05, base mean log2 expression≥10.) (Middle) Heatmap of differentially accessible peaks (*FDR*<0.05, $|\log_2 FC|>1$) presented as in (**c**) for genes in K-means clusters 1 and 3. (Right) ATAC-Seq signal profiles across *Ifng* and *Gzma* loci. Peaks present in all differentiation states highlighted in blue, activation-induced peaks in pink.

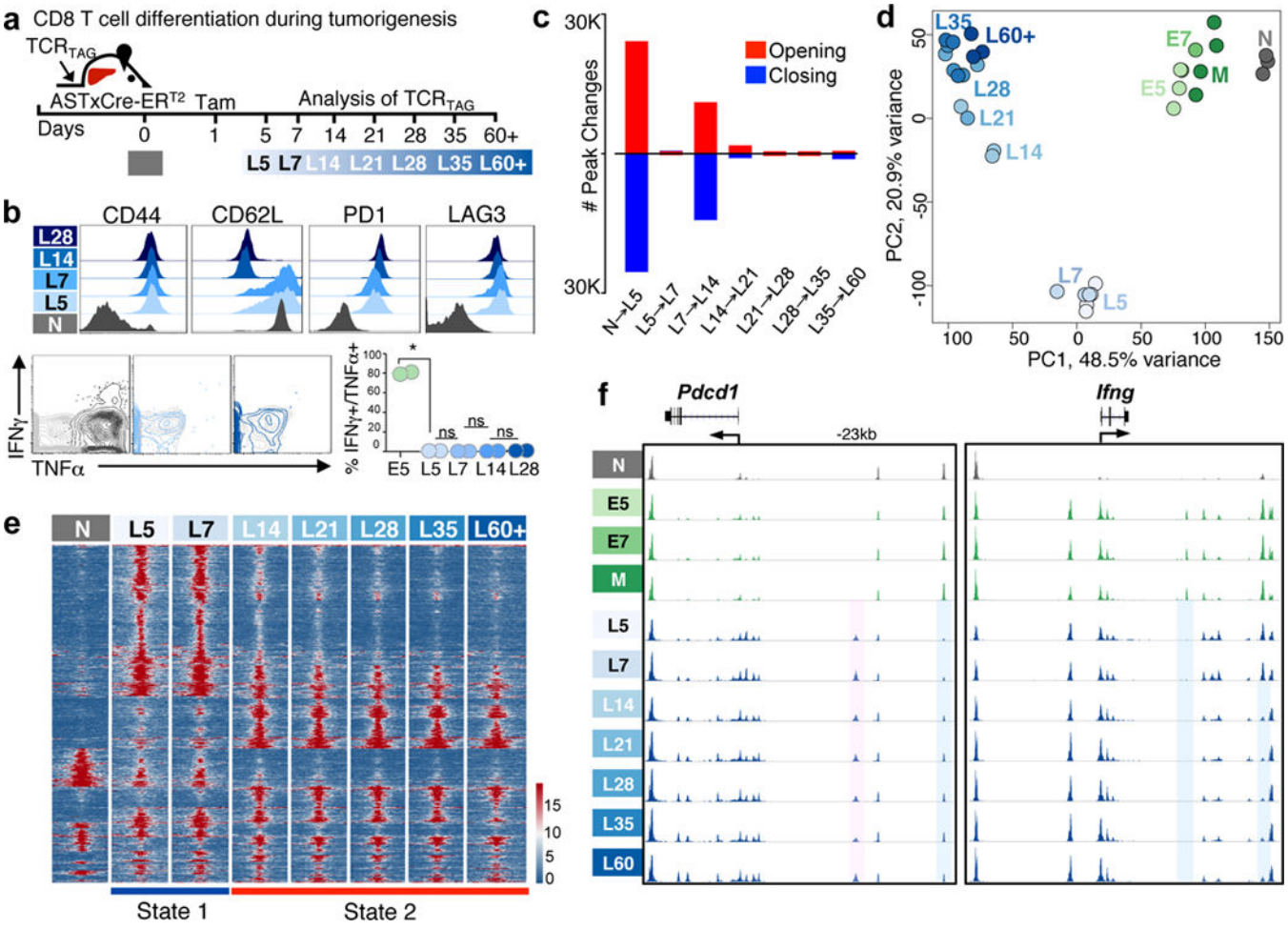

Figure 2. TST differentiate to dysfunctionality in developing tumors through discrete chromatin states

a, Experimental scheme. **b**, Immunophenotype and cytokine production (grey, no peptide control) (n=8 total, with n=2 per time point). Each symbol represents individual mouse. Representative of 5 independent experiments; mean ± s.e.m shown. **P*=0.0002 (Student's *t*-test); n.s. = not statistically significant. **c**, Number of peak changes during each transition (*FDR*<0.05). **d**, Principal component analysis (PCA) of peak accessibility in naïve TCR$_{TAG}$ (N; grey) during normal differentiation (green) and during tumorigenesis (blue). Each symbol represents single biological replicate. **e**, Chromatin accessibility heatmap (15,275 differentially accessible peaks as in Fig. 1c). **f**, ATAC-Seq signal profiles across *Pdcd1* and *Ifng* loci. Peaks uniquely lost (blue) or gained (pink) in TST.

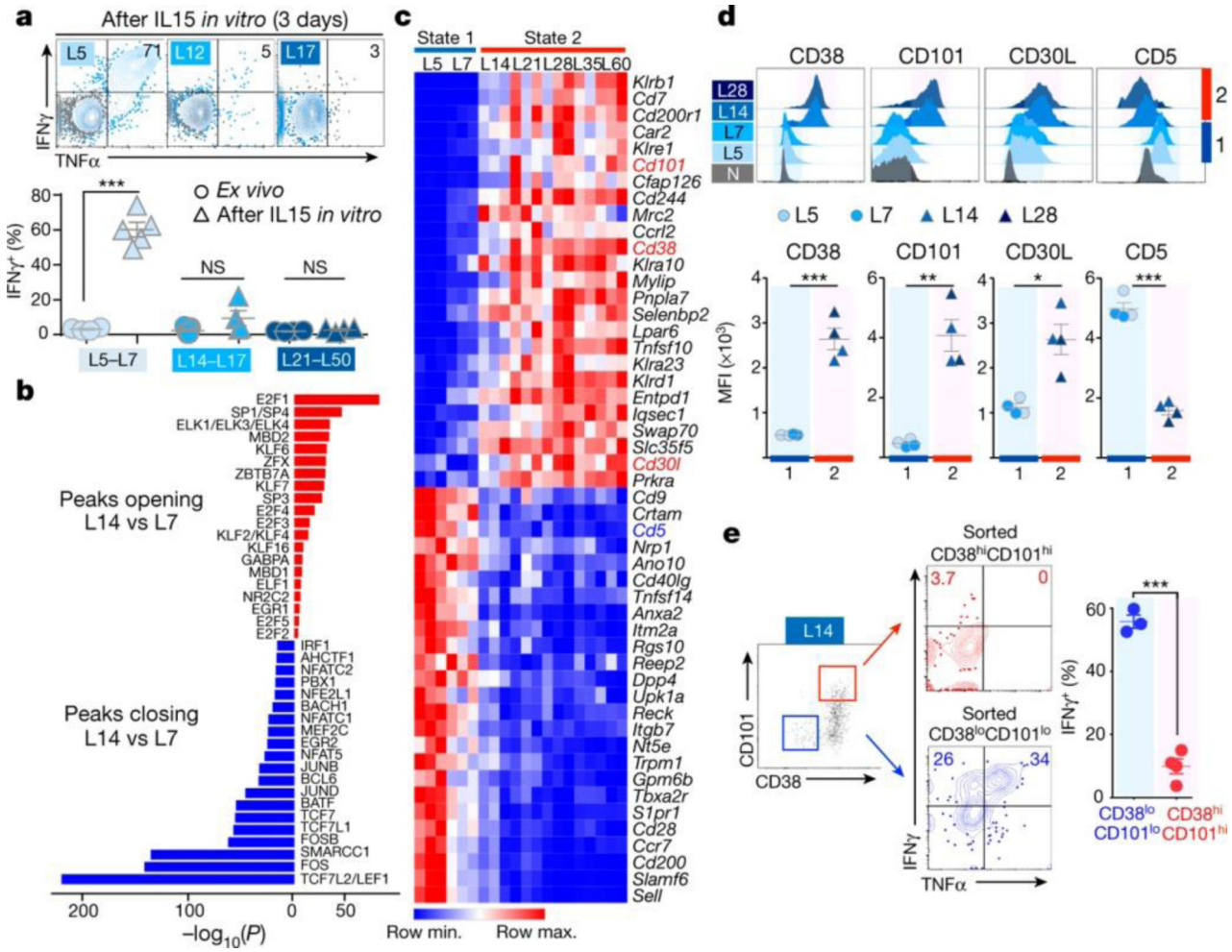

Figure 3. Discrete chromatin states correlate with reprogrammability and surface protein expression profiles

a, (top) Cytokine production by L5, L12, and L17 after 3 days *in vitro* IL-15 culture (grey, no peptide control); (bottom) IFNγ production straight *ex vivo* (circles) or after 3–4 days IL-15 *in vitro* culture (triangles). Pooled from 3 experiments. **b**, Top 20 most-significantly enriched TF motifs in peaks opening (red) and closing (blue) between L7 and L14. **c**, RNA-Seq expression (row-normalized) for most differentially-expressed genes encoding membrane proteins. **d**, CD38, CD101, CD30L and CD5 expression. Representative of 3 independent experiments. **e**, Cytokine production by sorted $CD38^{lo}/CD101^{lo}$ (blue) and $CD38^{hi}/CD101^{hi}$ (red) L14 after 3 days IL-15 *in vitro* culture. Similar data obtained with sorted L10 in independent experiment. (a, d, e) Each symbol represents individual mouse. Mean ± s.e.m. shown; **P*=0.005, ***P*=0.0005, ****P*≤0.0001 (Student's *t*-test).

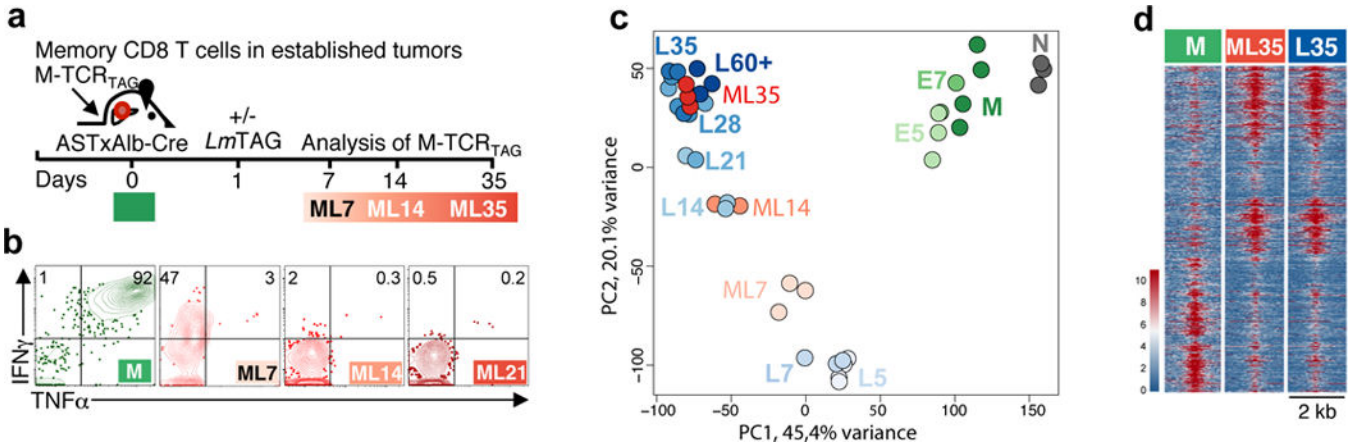

Figure 4. Memory TST rapidly enter the fixed dysfunctional chromatin state in established tumors

a, Experimental scheme. **b**, Cytokine production of M isolated from liver tumors. **c**, PCA of peak accessibility in TCR_{TAG} during acute infection (green), tumorigenesis (blue), and memory TCR_{TAG} in established tumors (red). **d**, Chromatin accessibility heatmap showing M, M re-isolated at D35 from established HCC tumors (ML35), and naïve TCR_{TAG} isolated at day 35 (L35) from early malignant lesions (see Fig. 2). Each row represents one of 19,679 differentially accessible peaks as in Fig. 1c.

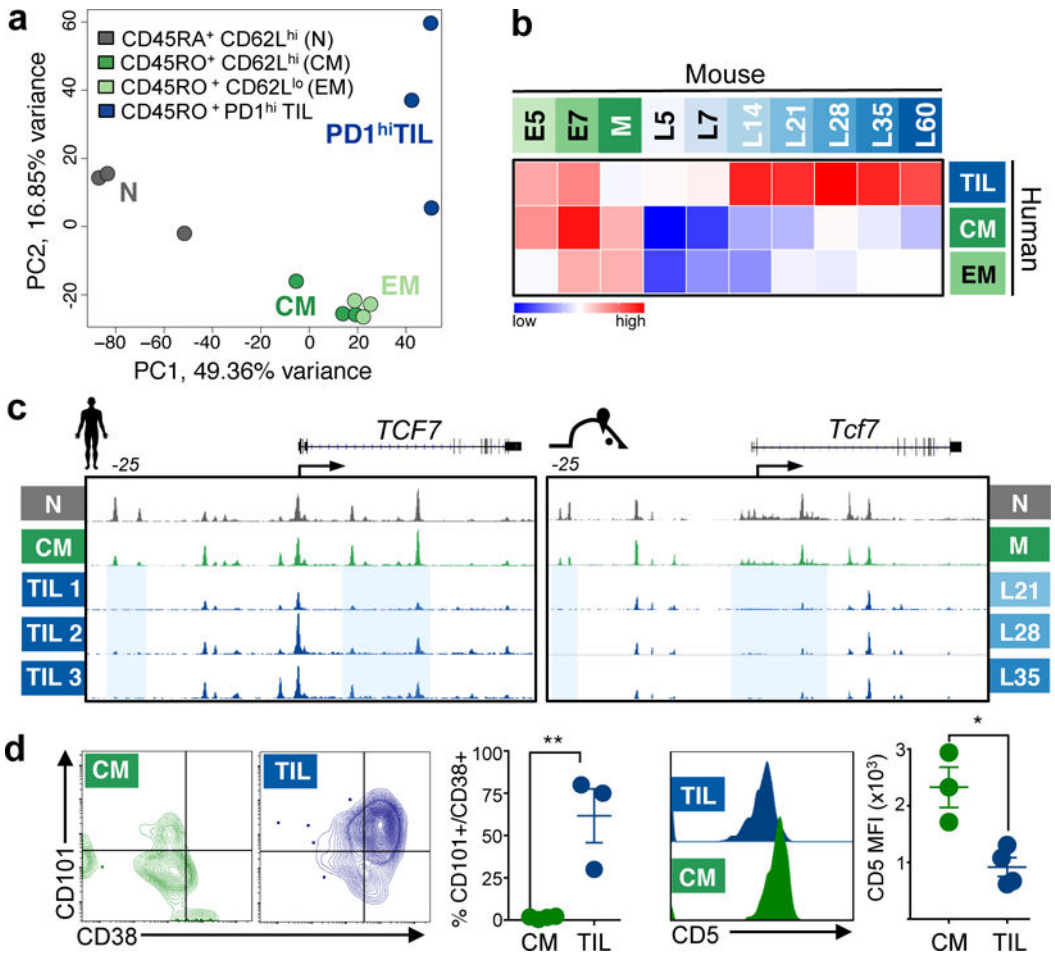

Figure 5. Human tumor-infiltrating PD1-high CD8 T cells enter a similar chromatin accessibility state as murine fixed dysfunctional TST

a, Peak accessibility PCA on human healthy donor PBL and PD1^{hi} TIL from melanoma and NSCLC tumors. **b**, For non-promoter peaks, normalized Spearman correlations of log_2FC calculated between human N and EM, CM or PD1^{hi} TIL versus log_2FC between murine N and E5, E7, M, and L5 to L60. $P<10^{-16}$ for all comparisons between human PD1^{hi} TIL and mouse L14 - L60. **c**, ATAC-Seq signal profiles across human *TCF7* and mouse *Tcf7* gene loci; peaks ost in human PD1^{hi} TIL and mouse L21, L28, L35 highlighted in blue. **d**, CD38, CD101 and CD5 expression on human CM (green) and PD1^{hi} TIL (blue). Each symbol represents individual healthy donor or patient. Mean ± s.e.m. shown; *P=0.01, **P=0.006 (Student's t-test).